

POLITECNICO DI TORINO

Master's Degree in Nanotechnologies for ICTs



Master's Degree Thesis

Development of a Sunlight Digitizer Applied to an Ultra Low Power Infrared Sensor for Crop Applications

Advisors

Prof. Matteo RINALDI

Prof. Matteo COCUZZA

Prof. Zhenyun QIAN

Candidate

Matilde Maria PAVESE

September 2020

Summary

The population driven need for food in the world will increase by 70% by 2050, while less land and natural resources such as water are available for farming. Therefore, increasing the efficiency of food production is incredibly important. Genetic studies suggest that the current production yield of crops has significant room to improve [1]. State of the art technologies cannot be used to implement such a continuous monitoring of large-scale crop fields. Commercially available sensors continuously consume power to monitor the environment even when there is no relevant data to be detected which limits their lifetime and results in unsustainable costs of deployment and maintenance (i.e. batteries need to be replaced every few weeks). The ARPA-E team, the very same project of which this master thesis is part of, realized a new class of zero-power and low-cost sensors. They are capable of monitoring the water stress related infrared characteristics of plants (i.e. leaf temperature and reflectivity) in the crop field and communicating wirelessly with the irrigation system control center upon the detection of irrigation indicators. The starting sensor of this master thesis is the one by Qian et al. [2], with some major contributed changes. Nevertheless, this new MEMS is still not able itself to be exploited in in-field applications. It needs a new system, the so called *sunlight digitizer*, to verify that the sensor is communicating a need-of-water because the plants actually requires water and not only because the irradiance of a day is too high. This last phenomenon would cause the reflectance of the leaf to be over the threshold, activating the sensor to send a need-of-water signal which is in reality a false alarm. Within this project such a digitizer is designed and simulated with *LTSpice*. Firstly, the simulations of the circuit show positive feedbacks. Secondly, a different schematic is simulated for the optimization of the solar cell. Then, the circuit is built and tested in the form of a breadboard. The use of a millimetric solar cell to supply the whole circuit is to keep on the philosophy of this project, the ultra-low power feature. The final results lead to the realization of a 1% irradiance window digitizer, i.e. the circuit provides a *within* signal set to high only when the irradiance of the sun is from 220 to 222 W/m^2 . This range is modifiable according to the sunlight conditions, i.e. to the average irradiance in which the digitizer is used. This can be easily done turning the knob of a potentiometer.

Acknowledgements

I would like to thank Professor Matteo Rinaldi, the Principal Investigator of Northeastern Sensors and NanoSystems Laboratory in which I had the pleasure to perform my Master Thesis, who gave me this priceless opportunity.

A great thank you goes to Professor Zhenyun Qian, for his kindness, comprehension and knowledge, mostly during this period of uncertainty. He proposed me a project in which I could better spend myself on.

I would like to acknowledge Professor Matteo Cocuzza for his endless availability and for having followed me in each step until here.

I would like to deeply show my gratitude to Politecnico di Torino and EDISU for their economic help, without it many students could not afford experiences like the ones I had the chance to live.

I wish to show my gratitude to Vageeswar Rajaram, for his daily support, for having me guided in this path, for giving me the enlightenings to make ring a bell.

I also would like to thank my lab mates: Antea, Sila, Jhaxing and Ryan. I wish I will have the chance to work with you again and also thank Wenjun, for her restless managing work to get the lab crew back at work as soon as possible.

I did appreciate the company of my housemates Dario, Fabio, Gabriel, Marisa and Matteo throughout these crazy months and a lovely thank you to the friends I met during these five years.

To my daddy and Dodo, who gave a meaning to the word *home*.

To Marco. Happiness is real only when shared.

Table of Contents

List of Tables	VIII
List of Figures	IX
Acronyms	XI
1 Introduction	1
1.1 The Laboratory	1
1.2 Presentation of the OPEN Project	2
1.3 The Sensor Design	5
1.4 Temperature-Based Sensor	11
1.5 Reflectance-Based Sensor	14
1.6 Other Applications	16
2 State of the Art	17
3 Methods	22
3.1 Option One	23
3.1.1 Components	24
3.1.2 Simulations Results	35
3.1.3 Breadboard Testing Results	36
3.1.4 PCB Testing Results	43
3.2 Option Two	46
3.2.1 Simulation Results	48
3.3 Option Three	49
4 Conclusions	51

4.1	Final Results	51
4.2	Next Steps	53
4.2.1	Packaging	53
4.2.2	Change of Etching	54
4.2.3	Finalization of the Circuit	54
A	Side Work - Connection of a Water Pump to the IR sensor	55
B	Paper	60
C	Matlab Minicode	68
	Bibliography	69

List of Tables

1.1	Threshold powers at different distances, which is calculated in Appendix C	8
2.1	Advantages and disadvantages of different infrared sensors	18
2.2	Different kind of actuations	19
2.3	State of the art water-stress plant detectors	21
3.1	Solar cell datasheet features [19]	25
3.2	Voltage regulator datasheet features [24]	30
3.3	Output of the solar cell at the desired irradiance	32
3.4	Window comparator datasheet features [26]	32
3.5	Values of resistor of the voltage divider	34
3.6	Comparison of quiescent currents between datasheet and simulations	36
3.7	Comparison of stand-by power consumption between datasheet, simulations and testing	42
3.8	Comparison of stand-by power consumption between datasheet, simulations and both testing phases	46
3.9	Comparison of the XOR IC used for testing and for simulations . .	47
3.10	Advantages and disadvantages of the three options	50
A.1	<i>TPS22860</i> datasheet specifications	56
A.2	Bias voltage changing with the RWC	58
A.3	Quiescent currents when the pump is connected to the IR device and when it is connected to its own batteries	59

List of Figures

1.1	ISEC building	2
1.2	Proposed technology platform schematic	3
1.3	MEMS design	5
1.4	Different phases of RWC calculation	7
1.5	Reflectivity Spectrum of different leaves	7
1.6	Emission spectrum for a leaf	8
1.7	Current across the switch as the heater is turned on and off	9
1.8	Deluxe smart grow closet	12
1.9	RWC and temperature of the leaf changing with the time	12
1.10	Setup to detect temperature change with RWC changing	13
1.11	Schematic setup for temperature-base water stress sensor	13
1.12	Reflectance change versus time	14
1.13	Schematic setup for reflectance-based sensor	14
1.14	Experimental and literature results of the reflectivity of <i>Glicine Max</i>	15
1.15	Reflectance and state of the switch versus the RWC	15
3.1	Irradiance versus daily hour. Concept on the left and data analysis on the right	23
3.2	Conceptual schematic of the sunlight digitizer	24
3.3	LTSpice Schematic for the option 1	24
3.4	Solar cell electrical circuit	25
3.5	Sweep to determine Number of Diodes - SC current versus OC voltage	26
3.6	Comparison between datasheet curve and my solar cell model	27
3.7	Irradiance-Voltage curve of the solar cell	27
3.8	Irradiance-Current curve of the solar cell [21] vs Open Circuit voltage	28
3.9	Solar Cell Complete Schematic	29

3.10	Output of the regulator vs output of the solar cell	30
3.11	Regulator analog circuit	31
3.12	Comparator block diagram	33
3.13	Components packages	34
3.14	Output of the comparator vs irradiance	35
3.15	Input current of the <i>LT1307</i> voltage regulator versus time	36
3.16	Input current of the <i>LTC1042</i> window comparator versus time	36
3.17	Picture of Circuit 1	38
3.18	Picture of Circuit 2	39
3.19	Lights setup	39
3.20	Output of the solar cell	40
3.21	Within signal high	40
3.22	Noise of the <i>width</i> signal	41
3.23	Voltage window of the comparator during the breadboard testing	42
3.24	<i>TPS61096</i> regulator schematic and PCB	43
3.25	<i>LTC1042</i> comparator schematic and PCB	44
3.26	Soldered PCBs	44
3.27	<i>width</i> signal	45
3.28	Voltage window achieving the 1% window	45
3.29	Schematic of Option 3	46
3.30	<i>LTSpice</i> schematic of the XOR implementation	47
3.31	<i>LTSpice</i> actual schematic for the XOR implementation	48
3.32	<i>LTSpice</i> simulation of XOR IC output vs irradiance	49
3.33	Schematic of Option 3	49
3.34	Normally closed switches technique	50
4.1	I-V curve of the solar cell, results of the <i>LTSpice</i> simulation	52
4.2	Breadboard complete setup	52
4.3	On the left, near zero power IR Wireless Sensor Node (WSN) circuit schematic and image. On the right, image of an RFID sensor tag	54
A.1	Conceptual schematic of the system	55
A.2	The three PCBs soldered together	57
A.3	Conceptual (on the left) and real (on the right) setup	57
A.4	Current consumption when the pump is OFF and ON	59

Acronyms

ARPA-E Advanced Research Projects Agency - Energy

COTS Commercial Out of The Shelf

DARPA Defense Advanced Research Projects Agency

DC Direct Current

DRIE Deep Reactive Ion Etching

FB FeedBack

FET Field Effect Transistor

FLIR Forward Looking InfraRed

GPIO General Purpose Input Output

HF High Frequency

IC Integrated Component

IR InfraRed

ISEC Interdisciplinary Science and Engineering Complex

LCC Leadless Chip Carrier

LED Light Emitting Diode

LS Load Switch

MEMS Micro-Electro Mechanical Systems

MIDC Measurement and Instrumentation Data Center

MPP Maximum Power Point

MWIR Medium Wavelength InfraRed

NEP Noise Equivalent Power

NEMS Nano-Electro Mechanical Systems

NSaNS Northeastern Sensors and NanoSystems

OC Open Circuit

PCB Printed Circuit Board

PIR Passive Infrared Sensors

PMP PhotoMechanical Photoswitch

PWM Pulse Width Modulation

RF Radio Frequency

RFID Radio Frequency Identification

RWC Relative Water Content

SC Short Circuit

SNR Signal to Noise Ratio

SWIR Short Wavelength InfraRed

TCR Temperature Coefficient of Resistance

WSN Wireless Sensor Node

Chapter 1

Introduction

1.1 The Laboratory

The entirety of this master thesis has been developed thanks to Northeastern Sensors and Nano Systems Laboratory (NSaNS) and guided by Professor Matteo Rinaldi. NSaNS Laboratory is a reality born almost 10 year ago in Boston, at Northeastern University, located in 805 Columbus Avenue in the new Interdisciplinary Science and Engineering Complex (ISEC) building, in Figure 1.1. The main goal of the laboratory is the development of miniaturized, low power and high-performance sensors and radio frequency components. Its focus is on the understanding and exploiting of the fundamental properties of micromechanical structures and advanced nanomaterials to engineer new classes of Micro and Nano Electro Mechanical Systems (MEMS/NEMS) with unique and enabling features applied to the areas of chemical, physical and biological sensing and low power reconfigurable radio communication systems [3]. It counts on more than 20 stable researchers plus a continuous presence of visiting students. Professor Matteo Rinaldi is, moreover, director of the SMART center, which is a research center that gathers multiple smaller laboratories. Their aim is to conceive and pilot disruptive technological innovation in smart devices and systems to make everyday life safer, easier and more efficient, in collaboration with federal agencies and industries. The OPEN project of which this master thesis is part is an example because it is funded by the Advanced Research Projects Agency-Energy (ARPA-E), a federal agency focused on high impact energy technologies. The team of which I am part of is the Plasmid team. The team is a subgroup of the NSaNS laboratory and it is in charge of the ARPA-E project. Alongside this master thesis, multiple projects are carried out by the group. As an example of the cooperation within the team, I gave my personal contribution to one of these projects, explained in details in Appendix A.

1.2 Presentation of the OPEN Project

Every second 127 new devices are connected to the web worldwide. At the end of 2020, the number of connected devices is expected to reach 37 billion [2]. The need to reduce their power consumption and dimensions several orders of magnitude is crystal clear in order to allow this permanently increasing number to reach 75 billions by the end of 2025 without catastrophic consequences. On the other hand, the population need for food in the world will increase by 70% by 2050, while land and natural resources such as water will constantly be less available for farming. Moreover, the soil quality will degrade with global warming. Therefore, increasing the efficiency of food production is incredibly important to avoid hunger in massive areas of the planet. Multiple studies suggest that the current production yield of crops has significant room to improve. The average yield achieved in commercial farms is only one tenth of the theoretical maximum, and less than half of the one demonstrated in trial fields [1]. The capability of acquiring comprehensive and real-time data of plants health and environmental conditions during growth with high granularity and translating it in easy instructions for the farmers would maximize the crop yield while conserving natural resources. State of the art systems can not be exploited for such purpose because they constantly consume power to monitor the environment even when there is not relevant data to be monitored, resulting in short lifetime of the device and in unsustainable costs of power and maintenance (e.g. substitution of batteries every few weeks or months), as it is explained in details in Chapter 2.

Farmers have to take typically about 40 yield impacting decisions each season, whose results can impact on a 10% positive or negative yield swing [1]. There

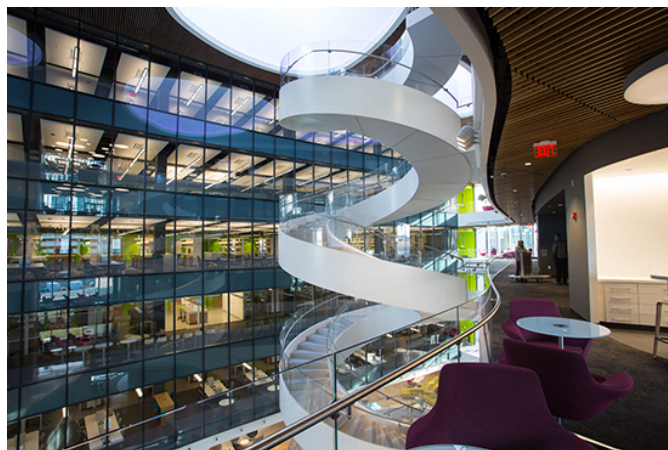


Figure 1.1: ISEC building

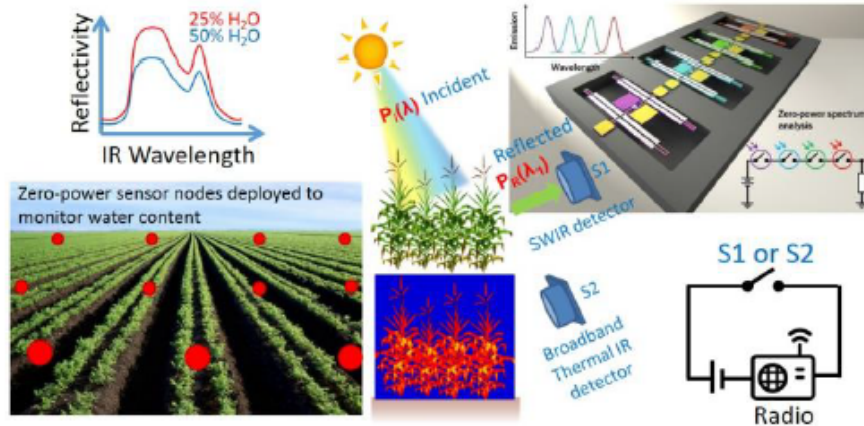


Figure 1.2: Proposed technology platform schematic

is a clear need to develop innovative technology platforms and decision support tools that maximize sustainable economic returns by increasing yields, conserving resources, and creating new market opportunities. The overall challenge is to monitor the physical, environmental and biological conditions that limit growth with high spatial and temporal resolution throughout production cycle and to identify interventions that relieve those constraints. Recent advancements in sensing technologies have now made it possible for biologists to extract massive volumes of genetic, physiological, and environmental data from certain crops in relatively small test fields.

The purpose of the OPEN project of the SMART laboratory, of which this master thesis is part of, is to develop an in-field spatio-temporal monitoring system of water content in plants. It consists in a distributed network of zero power sensors that are capable of capturing, storing, communicating and processing the in-field data, ultimately determining the actions farmers should take to maximize the yield. This new monitoring system is a step forward in the direction of reducing the power consumption of connected devices and of maximizing crops yield. This new class of zero power and low-cost hyperspectral sensors are capable of monitoring the water stress related InfraRed (IR) characteristics of plants (e.g. leaf temperature and reflectivity) in the crop field and communicating wirelessly with the irrigation system control center upon the detection of irrigation indicators. Differently from the current state of the art, the new sensors by Qian [2] based on micromechanical structures, utilize the energy of the IR radiation emitted or reflected from the leaves of plants to detect their surface temperature or spectral reflectivity, respectively, and compare them to the pre-determined threshold, as explained in Chapter 3, without consuming any electrical power during standby mode. The sensors wake up (i.e. drain power from the battery) only upon detection of changes in the irrigation

indicators above alarming thresholds and then they transmit a radio frequency signal indicating the need of irrigation. The complete elimination of the standby power consumption results in a nearly unlimited duration of operation, saving the maintenance costs associated with frequent battery replacements. The sensors are able to wirelessly reveal thousands of irrigation needs without ever replacing the sensor coin battery. Thus, the life time is extended to ~ 10 years, limited only by the battery self-discharge. The project delivers a fundamental building block for a visionary world in which the farm produce is more efficient, sustainable, and resilient by leveraging technological advancements. The main steps of the OPEN project are:

1. Design and demonstrate a zero power leaf temperature sensor, working in the Medium Wavelength Infrared Range (MWIR) capable of detecting a 5°C temperature variation in a area of $\sim 1\text{ m}^2$ within a 1 m distance from the sensor.
2. Design and demonstrate a zero power leaf reflectivity sensor, working in the Short Wavelength Infrared Range (SWIR) ($1.3 \div 2.8\ \mu\text{m}$), capable of detecting 10% increase in reflectance of leaf surface (corresponding to $\sim 20\%$ decrease in water content) when the leaf is directly illuminated by a predetermined radiation intensity (i.e. calibrated impinging IR radiation from sunlight or other sources).
3. Determine the best practice for water content monitoring in field by investigating the detection probability and false alarm rate of each approach and the combined solution.
4. Design and develop vacuum packaging, low power wireless module, optical components, housing and supporting mechanics (for potential field deployment) for the wireless sensor node.
5. Demonstrate a complete wireless sensor node capable of communicating wirelessly with the irrigation system control center receiver upon the detection of irrigation indicators. The sensor can reveal thousands of irrigation needs while maintaining a low false alarm rate without ever replacing the sensor coin battery. The life time is extended to ~ 10 years, limited by the battery self-discharge.

Parts of Point 1 and Point 2 have already been achieved partially by the Plasmid laboratory before the beginning of this master thesis and are presented in details

in Section 1.4 and 1.5 of this chapter, while the remaining parts of Point 1 and Point 2 are the focus of this master thesis.

1.3 The Sensor Design

In Figure 1.3, a general view of the MEMS design developed alongside the project, is shown. The Photo Mechanical Photoswitch (PMP) consists of two symmetric released cantilevers facing each other. Each cantilever is composed of a head, an inner pair of thermally sensitive bimaterial legs (Aluminum and Silicon Dioxide, respectively Al and SiO_2), an outer pair of temperature- and stress-compensating bimaterial legs connected to the substrate and a pair of thermal isolation links between the inner and outer bimaterial legs. A plasmonic infrared absorber is integrated in the head of one cantilever, the absorber one, whereas the head of the other cantilever is covered by a 150 nm Gold (Au) reflector. The absorbing head also carries a high-stiffness bowl-shaped Platinum (Pt) tip electrically connected to one of the device terminals, whereas the contact pad connected to the second terminal is defined on the opposite reflecting head. The metal tip and the contact pad are separated by a ~ 500 nm air gap. On the absorber head, an array of lithographically defined plasmonic nanostructures is placed. The nanostructures collect the incoming IR radiation and, changing the dimensions and the distances between them, a narrow or a broadband range can be obtained. The bimaterial legs, on the other hand, are useful to make the whole device insensitive to a room temperature change. Indeed, both the inner and outer pairs of legs bend in the same direction in response to ambient-temperature variations. Any residual ambient temperature- and/or stress-induced deflections of the two cantilevers are compensated by the symmetry of the structure, since both cantilevers deflect in the same fashion the designed gap dimension is preserved. The whole design consists in a total of 13 masks. When infrared radiation that matches the lithographically defined absorption band impinges on the top surface of the device, it is primarily absorbed by the plasmonic head and converted into heat, which leads to a temperature

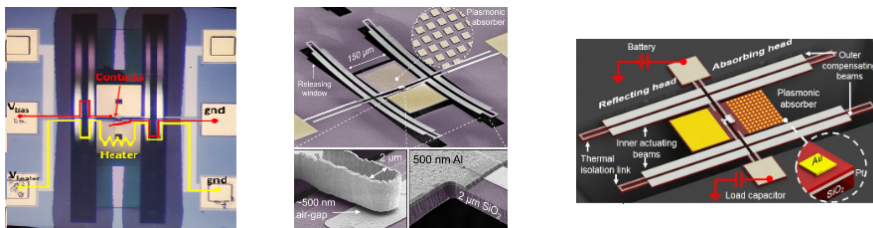


Figure 1.3: MEMS design

increase of the corresponding cantilever up to the thermal isolation. The infrared-induced temperature rise causes a downward bending of the corresponding thermally sensitive pair of bimaterial legs, which leads to a vertical displacement of the metal tip that brings it into contact with the opposite terminal (that is, the contact pad) when the absorbed infrared power exceeds the design threshold [2]. The main differences made to this sensor developed by Qian during the OPEN project are:

1. New heaters, under both the reflecting and the absorbing heads, useful to reset the device .
2. New pair of pads, to control both the upper and the lower heater from the external.
3. The absorber head has a reduced thickness to reduce the response time.
4. Optimized dimensions of the bimaterial legs to improve sensitivity.
5. Larger contact areas to allow threshold power scaling.

Basically, during the testing phase, it has been noticed that an artificial reset, i.e. an external voltage applied to the new pads, would fasten up the procedure of reset and would help the calculation of the threshold power intrinsic to the device. Once the radiation overcomes the threshold, the upper head bends and the contact is made. Due to still unknown causes, however highly probable due to an accumulation of charge, the head remains bent over even when the irradiation is no longer above the threshold. This is why the heaters have been added to the old design. When an external voltage is applied, the metallic serpentine below the head warms up causing the contact previously established to break. This allows the device to bend again once in the predefined conditions.

Another main aspect of the new design is the lithographically defined absorber head. The head differs between the reflectivity-based water stress sensor and the temperature-based one. As far as the former is concerned, the plasmonically enhanced absorbers are defined to collect irradiation at $1.5 \mu m$ with a $150 nm$ bandwidth. This value corresponds to the wavelength at which the reflectance spectra of a leaf presents a valley. Before carrying on with the illustration of the differences, a small paragraph has to be dedicated to the definition of the Relative Water Content (RWC). The RWC is probably the most appropriate measure of plant water status in terms of the physiological consequence of cellular water deficit [4]. Its formula is:

$$RWC = \frac{W - DW}{TW - DW} \cdot 100 \quad \% \quad (1.1)$$

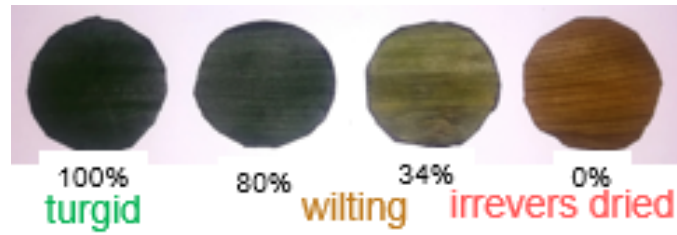


Figure 1.4: Different phases of RWC calculation

where W is the weight of the freshly cut leaf, DW is the weight of leaf disc dried at $80\text{ }^{\circ}\text{C}$ for 24 h and TW is the weight of the leaf disc floating on de-ionized water in a closed petri dish. Full turgidity is reached within $3\text{--}4\text{ h}$ under normal room light and temperature. The leaf disc is assumed to be 1.5 cm in diameter, avoiding large veins. In Figure 1.4, the different phases of a *Glycine Max* leaf during the RWC calculation process is shown.

Going back to the reflectivity-based sensor, the reflectance value corresponding to the wavelength at which the reflectance spectra of a leaf presents a valley change accordingly to the RWC, as depicted in Figure 1.5. This is because such point in the spectrum corresponds to the water absorption wavelength. When the RWC of the leaf is higher, the reflectivity is lower because the water contained in the leaf absorbs the impinging irradiation. On the other hand, the smaller the RWC, the

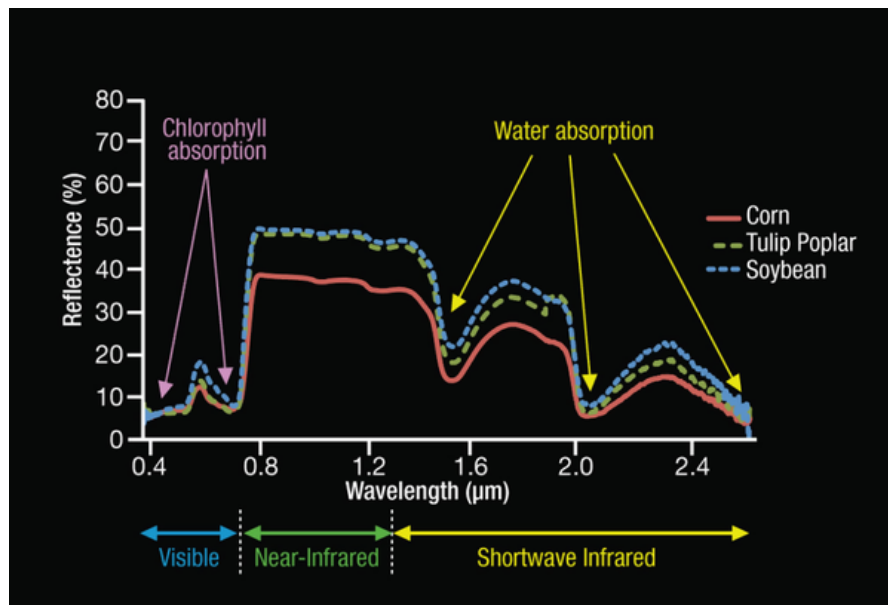


Figure 1.5: Reflectivity Spectrum of different leaves

	Threshold Power at 1 m	Threshold Power at 5 m
Reflectance-based	300 <i>nW</i>	5 <i>nW</i>
Temperature-based	60 <i>nW</i>	3 <i>nW</i>

Table 1.1: Threshold powers at different distances, which is calculated in Appendix C

higher the reflectivity. As shown in Figure 1.5, there are multiple water absorption valleys, but the one which presents more ΔR at different RWC is the one at around $1.5 \mu m$. Moreover, at this wavelength, the available power is higher. That is why the reflectance-based sensor is designed to absorb at $1.5 \mu m$ with a bandwidth of about $150 nm$.

A different wavelength is exploited for the temperature-based sensor. The leaf emits in a broadband spectrum; however, at $10.3 \mu m$ a greater difference in temperature for different RWC values is empirically calculated. Such a wavelength corresponds to the thermal IR emission peak of water-stressed plants. In this case a broader band of about $4 \mu m$ from 8 to $12 \mu m$ is needed, as shown in Figure 1.6. Due to these different aspects, the two devices require different threshold powers due to the contrasting incoming power. In Table 1.1, the threshold powers are reported, considering the leaf at $1 m$ and $5 m$ of distance from the sensor. At higher distance, the thresholds remarkably decrease because of the less impinging power. The

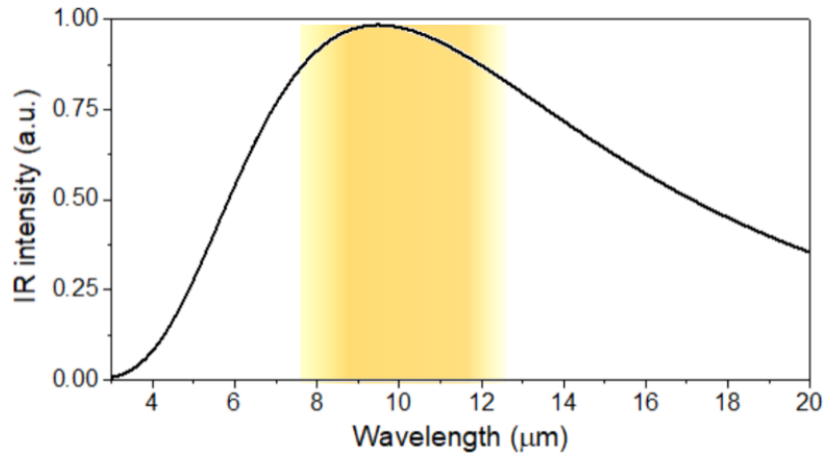


Figure 1.6: Emission spectrum for a leaf

formula for the calculation of the threshold power P_{th} is:

$$P_{th} = \frac{V_{heater}^2}{R} \quad (1.2)$$

where V_{heater} is the voltage applied at the heater pads (bottom ones) mentioned before and depicted in Figure 1.3, and R is the resistance of the heater serpentine, which is $63.8 \text{ k}\Omega$. V_{heater} is increased until the power dissipated as heat is sufficiently high to actuate the contacts and close the switch. It has to be noticed that the device is tested in a vacuum probe station to ensure that there is no heat loss through convection in air. The status of the switch, during this process, is monitored continuously by applying a separate bias V_{bias} across the switch terminals (in the middle pads) and measuring the current using the source meter by *Keithley*, model 2450. In Figure 1.7, the measured current across the switch is shown as the heater is turned on and off with a V_{heater} that corresponds to a power just above P_{heater} . When triggered on, the current changes with a conductance ratio of more than 4 orders of magnitude from $\sim 0.1 \text{ nA}$ to $0.7 \text{ }\mu\text{A}$ for a V_{bias} of 10 mV (the non-zero off current is due to instrument noise). This essentially demonstrates the zero subthreshold leakage of the switches, which is a key factor for zero standby power consumption. $P_{threshold}$ is 492 nW for this particular tested device.

Up to now, such small thresholds as reported in Table 1.1, have not been achieved yet. However, the issue can be easily solved in two different manners. The first

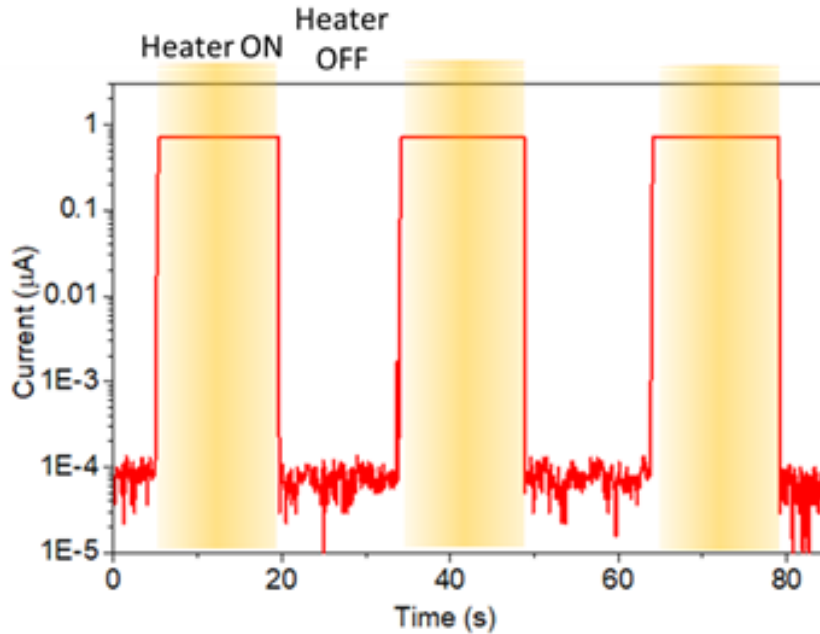


Figure 1.7: Current across the switch as the heater is turned on and off

way is to place a Fresnel lens on the top of the vacuum chamber where the device is positioned. Its aim is to collect and concentrate the incoming power. The lens by *Edmund Optics* has a diameter of 2 cm and a focal length of 1.4 cm, providing a 70 times magnification in the wavelength range of interest. Both the lens and the window of the vacuum chamber are made of Calcium Fluoride (CaF_2) in the reflectance-based sensor, which is a material transparent in the SWIR. They are made of Zinc Selenide ($ZnSe$) for the temperature-based one, transparent in the MWIR. The second way is thanks to the application of a bias voltage that is useful to achieve such small threshold powers. Applying this bias voltage causes an electrostatic force to appear across the contacts, leading them to move towards each other and thus reduces the gap. The gap reduces until the point where the electrostatic force is canceled out by the spring force generated in the opposite direction by the cantilever beam. As a result, with a reduced contact gap, less actuation is required from IR power to trigger the switch. This effectively reduces the threshold. Furthermore, this technique is passive during standby since there is no current flow/power consumption when the contacts are at equilibrium. Thus, not only is it useful in improving threshold, but the bias voltage also acts as a simple tool to adjust the threshold post-fabrication, since the fabrication process itself can contribute to contact gap variations across the wafer. A model to predict the threshold of the switches for an applied bias was developed previously and experimentally validated using the previous generation of devices. The threshold power P of the switch for a given applied bias V_{bias} is given by:

$$P = P_0 \cdot \left(1 - \left(\frac{V_{bias}}{V_{pull-in}} \right)^{2/3} \right) \quad (1.3)$$

where P_0 is the threshold without an applied bias and $V_{pull-in}$ is the pull-in voltage when the switch is not exposed to IR. This scaling technique was experimentally demonstrated to provide a threshold scaling of more than 17 times over the unbiased case, as low as 20 nW.

Another important aspect that has a main influence on the power threshold is the contact gap, which is the distance between the absorbing and the reflecting head. A smaller one clearly leads to a lower threshold power, i.e. to a more sensitive device. The gap g is estimated using the pull-in voltage technique. Since the contacts are effectively a pair of capacitors with an overlap area A and vacuum as a dielectric, increasing V_{bias} causes charges to accumulate on either contacts. Because the contacts are attached to cantilevers (i.e. springs), the electrostatic force developed between the contacts due to these charges causes the contacts to move towards each other. At a certain voltage when V_{bias} equals $V_{pull-in}$, the system becomes unstable and the contacts snap closes (i.e. pull-in). The value of

this pull-in voltage is given by:

$$V_{pull-in} = \sqrt{\frac{8 \cdot k \cdot g^3}{27 \cdot \epsilon_0 \cdot A}} \quad (1.4)$$

where k is the effective stiffness of the cantilevers ($0.0075 \frac{N}{m}$ from simulations). By sweeping the voltage V_{bias} (without applying any heater power) until the contacts close, $V_{pull-in}$ can be measured and g can be readily calculated. The overlap area A ($67.7 \mu m^2$) is measured using an optical microscope at high magnification. For the tested device, $V_{pull-in} = 2.23 V$ and thus $g = 1.095 \mu m$. A sacrificial layer of $500 nm$ amorphous Silicon (Si) is deposited and the distance g between the two contacts is supposed to be the same. However, this is not what is calculated with Equation 1.4 from the measurements just cited. This issue is under investigation and may be solved exploiting different techniques of etching. The current method is with Xenon Difluoride (XeF_2) dry etch while Deep Reactive Ion Etching (DRIE) and wet etching can be exploited. At the same time, a voltage-bias based technique can be used to passively mitigate gap inconsistencies, for the same reasoning made previously for the threshold power calculation process (i.e. thanks to the heater). Also in this case, the process requires zero power during standby, since a voltage is applied but no current is flowing through the contacts.

1.4 Temperature-Based Sensor

The plant selected to perform all the laboratory testing is *Glicine Max*, also known as soybean, chosen for its numerous advantages and applications. Soybean is the most important protein source for feeding animals in farms, from its seeds oil can be extracted and it can also be consumed by humans (e.g. tofu, soy milk, soy sauce). Additionally, there is a lot of literature about its features. It is important to underline that *Glicine Max* is also the primary source of biodiesel in the USA since from a bushel of this plant, $5.68 L$ of biodiesel can be obtained [5]. Its dimensions allow the cultivation in a laboratory and its quick growth encourages the use of such a plant (~ 2 weeks to have leaves at least $1.5 cm$ in diameter). During the testing period, the plants are preserved inside a grow closet represented in Figure 1.8, suitable for maintaining good conditions during the life of the *Glicine Max* samples.

As a proof of the correlation between RWC and temperature, and to confirm the literature about it, additional tests are performed. The results are shown in Figure 1.9. In the plots, *wet boundary* means that the chopped leaf (always $1.5 cm$ in diameter) is put in deionized water the night before the testing, and *dry boundary* means that, at the end of the testing, the leaf is placed in the oven at $80 \text{ }^\circ C$ for a few hours and then tested again. The experimental and the schematic setup of the



Figure 1.8: Deluxe smart grow closet

temperature testing are shown in Figures 1.10 and 1.11, respectively. On the left of Figure 1.10, a 100% RWC 1.5 cm leaf disc is tested (supposing it is isothermal, i.e. it has a uniform emission spectra). The temperature of the leaf is 26 °C as detected by the Forward Looking InfraRed (FLIR) camera, and the MEMS switch does not close because the incoming radiation is not above the device threshold. Only a few hours later, as *Glicine Max* dries out very fast, the leaf reaches a RWC of 61%, as shown on the right of Figure 1.10. The detected temperature is now 29.6 °C, the power transmitted to the sensor is above the sensor threshold and the upper

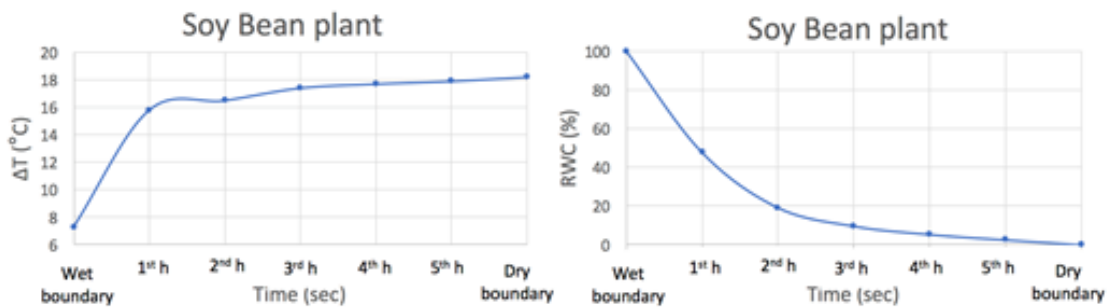


Figure 1.9: RWC and temperature of the leaf changing with the time

head is bent down. A LED indicator shows the occurred contact. It is important to notice that the temperature increases with a reduced RWC because the leaves stomata close themselves, resulting in a reduced evapo-transpiration, which raises the leaf temperature. Thus, Point 1 of Section 1.2 is proved successfully.

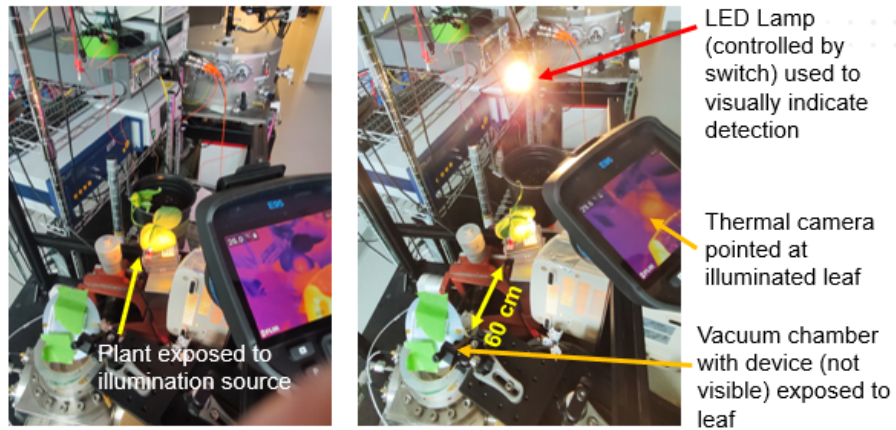


Figure 1.10: Setup to detect temperature change with RWC changing

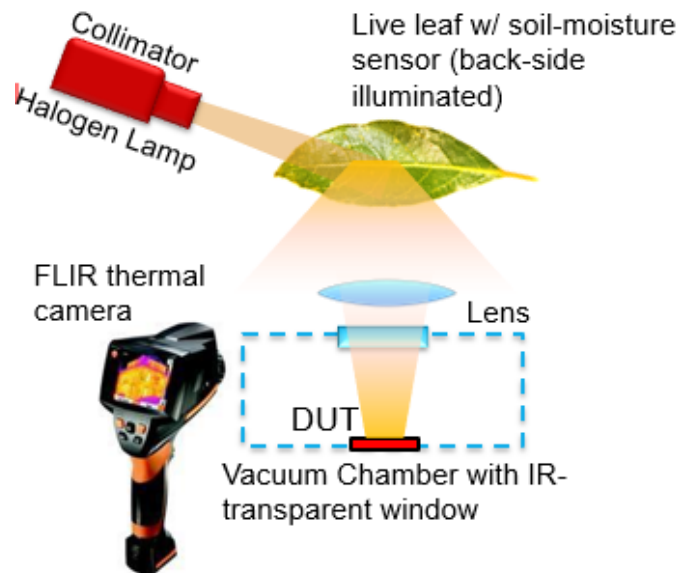


Figure 1.11: Schematic setup for temperature-base water stress sensor

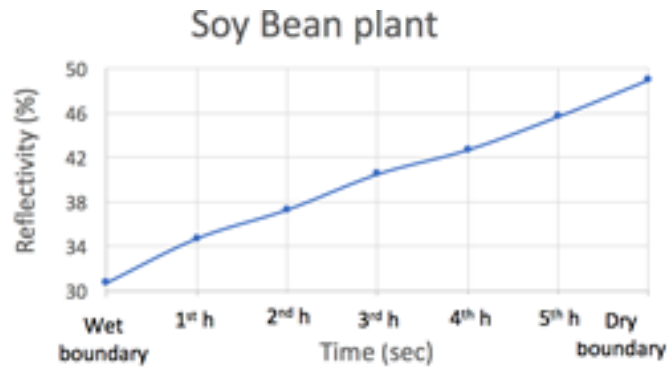


Figure 1.12: Reflectance change versus time

1.5 Reflectance-Based Sensor

As for the temperature-based water stress sensor, also the reflectance-based one is tested and its functioning is proved. First of all, a proof of concept to check the validity of the literature is done, following the same wet and dry boundaries procedure explained in Section 1.4. The results obtained are plotted in Figure 1.12. The sensor is tested accordingly to the schematic setup of Figure 1.13. In Figure 1.14, on the other hand, experimental results compared to the literature ones [6] are shown regarding the change in reflectance with different RWC (i.e. at different time of the day after stopping to water the plant). The power reflected by the leaf, with a RWC of 65.8%, results to be ~ 209 nW. A RWC of 65.8% is

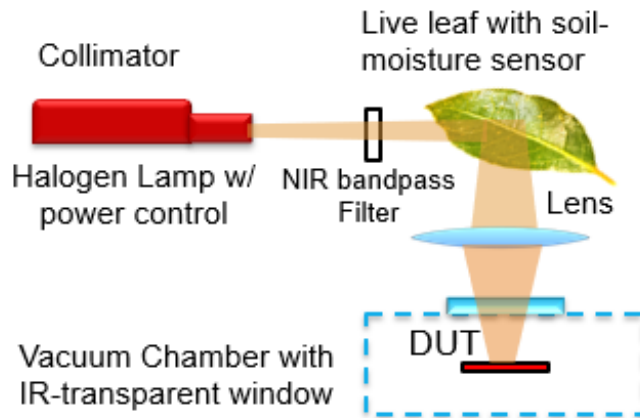


Figure 1.13: Schematic setup for reflectance-based sensor

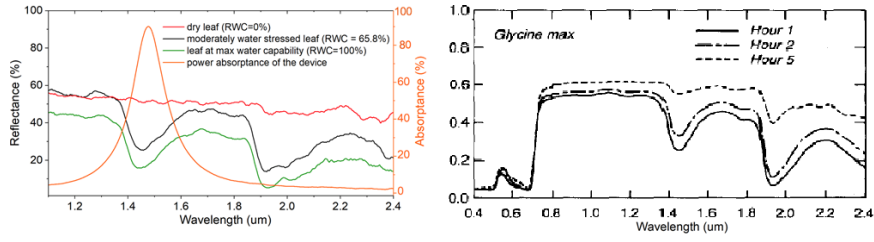


Figure 1.14: Experimental and literature results of the reflectivity of *Glycine Max*

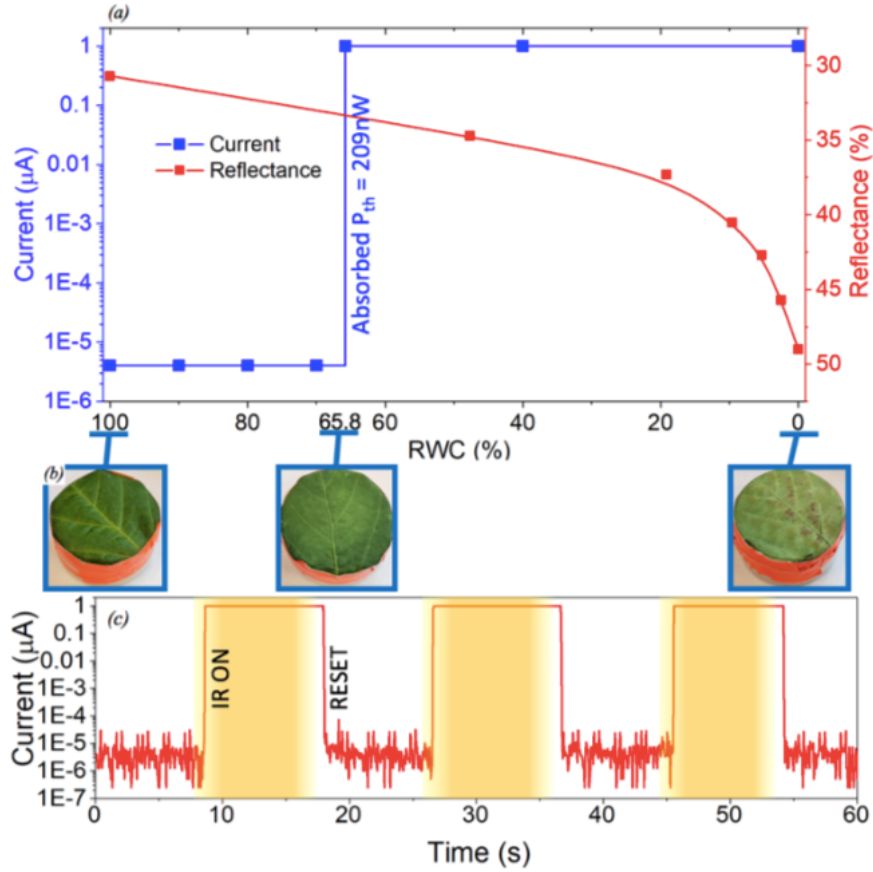


Figure 1.15: Reflectance and state of the switch versus the RWC

named *witting point*, because at that percentage value the plant can still resume. When the water content reaches a value lower than the *witting point*, the plant is considered dead. Thus, the sensor is set to have a power threshold of around 65.8%. As expected, although the reflectance change from 100% to 65.8% of RWC is small (ΔR of $\sim 3.4\%$), the device reliably turns on only when exposed to samples with $RWC \leq 65.8\%$, as shown in Figure 1.15.

The specific purpose of this master thesis is the completion of the reflectance-based sensor, whose functioning is already explained in details before. Since the intensity of the impinging sunlight radiation varies depending on the time of the day and the atmospheric conditions, an in-situ calibration technique is required to guarantee the zero power sensor to be operational only when exposed to a predetermined intensity of sunlight radiation. In other words, the goal is to develop a new system, which from now on will be called sunlight digitizer. The digitizer returns a high signal only and exclusively when the sun irradiance is within a defined range. This is important in order to turn the watering system on only when the leaves actually need water and to circumvent the case in which the reflectivity of the leaves is too high because of other circumstances, such as a very sunny day. The system is placed in series to the sensor.

1.6 Other Applications

The same sensor with minor modifications can be exploited for other applications, such as occupancy sensor and chemical detector. In particular, a project funded by Bill and Melinda Gates lead to the design and demonstration of a Volatile Organic Compounds detector [7]. The working mechanism is based on molecules of the chemical substances which lie over the top cantilever and cause bending. The device reaches a sensitivity as high as 5000 *ppm* of ethanol have been detected thanks to an about 20 μm displacement of the cantilever.

Chapter 2

State of the Art

Current state of the art sensors constantly consume power, also when there is no need to collect data, and they are not smart enough to select a target of interest. State of the art photoswitches are based on a photosensitive element to transform the impinging radiation in an electrical signal and then, with the help of active electronic components, to digitize this signal. Nevertheless, they still present multiple issues such as a finite sensitivity of the photosensitive element and the non-zero subthreshold conductance of the electronic components involved in digitizing the electric signal. Both these problems make the whole system burn a considerable amount of power.

Infrared sensors, main subject of this master project, usually exploit a pyroelectric material as photosensitive element (Noise Equivalent Power, NEP, of $1 \text{ nW}/\text{Hz}^{\frac{1}{2}}$) with one or more amplification stages and a comparator to digitize the signal. The amplifiers are necessary to achieve meaningfully low thresholds, in the order of hundreds of nW . Due to the power drained by the pyroelectric material and by the active elements, the power consumption can not be lower than tens of microwatt ($\sim 7 \mu\text{W}$). Other types of pyroelectric devices, like photon detectors and microbolometers, do exist with even lower NEP, but they are not implemented as Passive InfraRed (PIR) sensors due to their higher power consumption [8].

In photon detectors, the radiation is absorbed due to interaction with electrons. The electrical signal in output is the result of a change in the electronic energy distribution. Their main advantages are the fast response and the excellent Signal to Noise Ratio (SNR). The drawback is that these detectors usually require cooling since noise in photon infrared sensor increases exponentially with the temperature of the ambient. This makes them bulky, heavy, expensive and inconvenient to use for certain applications [9].

Thermal detectors are based on the principle that incident radiation, which is

Type of detector	Advantages	Disadvantages
Thermal (bolometer, thermopile, pyroelectric)	Light, Low cost Working at T_{room}	Low detectivity at HF Low response (ms)
Photon (intrinsic, extrinsic, free carriers)	Fast response Good SNR	Require cooling (bulky, heavy)

Table 2.1: Advantages and disadvantages of different infrared sensors

absorbed, leads to a change of the temperature. In this case, the measured electrical signal depends on the impinging radiation power itself. These devices can be wavelength dependent if proper design constraints are met (like wavelength dependent absorbers). Their strengths are the cost and the trivial usage, while the weakness is the need of being thermally isolated from the surrounding due to the temperature variation caused by incident radiation [9, 10]. Depending on the type of detector, different parameters are measured to define the performances of the detector itself: variation of electrical resistance in bolometers, induced thermoelectric voltage in a thermocouple and internal electric polarization in pyroelectric systems.

Up to 2017, only MEMS with thermal or metal-to-metal kinds of actuation have been studied. Going more into details of the first category, thermal detectors can in turn be divided in thermoelectric, pyroelectric and bolometers [11]. The temperature change in the thermoelectric sensors will become a voltage signal output through the Seebeck effect, while for the pyroelectric ones it corresponds to an accumulation of charge in the object which has been warmed up. For the last one in the list the change in temperature is detected through the variation of the electrical resistance of the system. The main features of these three different kinds of actuation are included in Table 2.2. On the other hand, concerning the other category of actuation, metal-to-metal Radio Frequency (RF) MEMS usually require relatively high actuation voltages to drive the movable part (order of magnitude in the units of V), making these devices not suitable for ultra-low power applications [12].

All the technological issues mentioned until now have been partially solved by micro-nano electromechanical relays because they rely on mechanical motion to make and break an electrical contact between two terminals. These systems, due to their nature, do not present sub-threshold conduction while they do provide extremely low leakage current and abrupt sub-threshold slopes. Therefore, they present all the necessary features to be used in zero-power consumption systems. In 2017, Qian et al. [2] demonstrated the first relays with light actuation. The new MEMS with this actuation relies on plasmonically enhanced thermomechanical

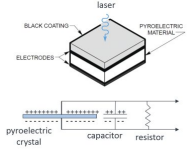
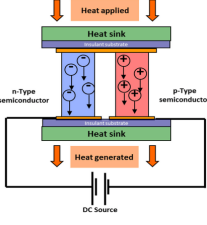
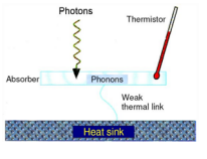
Transducers	Conversion Effect	Signal	Responsivity	Basic Design
Pyroelectric	Pyroelectric	SC current	Prop to $\Delta T/t$	
Thermoelectric	Seebeck effect	OC voltage	Prop to ΔT	
Bolometer	TCR	SC current and OC voltage	Prop to ΔT	

Table 2.2: Different kind of actuations

coupling to collect the impinging electromechanical radiation in a very specific region of the spectrum and exploits this energy to mechanically create a contact between two terminals without the need of any other power source. This fact leads directly to a zero-power consumed sensor, able to provide a reversible off-to-on transition (which corresponds to a digitized bit) when exposed to a light intensity that goes above a certain threshold [2]. The working region in the spectrum is lithographically defined by plasmonic nanostructures, which can provide both a narrowband and a broadband region where the device collects the light. IR-based relays can be used in the field of water content monitoring. These techniques are particularly attractive since they are non-destructive and can be completely automated requiring less complexity in measurement and data processing to accurately determine plant stress. Studies have shown that leaf moisture content is a direct indicator of plant stress that affects evapotranspiration and leaf reflectance in the SWIR ($1.3 \mu m \div 2.8 \mu m$) and MWIR ($4 \mu m \div 5.5 \mu m$) regions [13, 14, 15, 16]. The reduction in evapotranspiration is a result of stomatal closure in the leaves during stressed conditions, which also has a direct correlation with the temperature of the leaf by making it higher than the surroundings, up to $\sim 10 \text{ }^\circ C$. The measurement of such a temperature variation via IR thermal sensing has been used as a reliable indicator of plant water stress. The reduced water content in a leaf can also be sensed remotely by monitoring the spectral reflectance of the leaf in both SWIR and MWIR spectral regions because it increases with decreasing moisture content

[16].

Non MEMS IR-based methods use handheld devices (thermal and hyperspectral cameras), which are bulky, labor intensive (requiring advanced operator training) and extremely costly. Therefore, they cannot be effectively employed to continuously monitor large areas with high spatial resolution while ensuring a sufficient return of investment for the farmers. Satellite-based hyperspectral IR imaging is typically used to monitor larger areas. However, this approach is characterized by severely limited spatial and temporal resolutions (\sim weeks). Most recently, thermal and hyperspectral IR cameras combined with unmanned aerial vehicles have been employed for imaging large area of crop field from the air. Nevertheless, the costs involved with this approach are prohibitive for frequent inspections throughout the production cycle. Moreover, further data processing and interpretation by experts are required to make decisions on the most effective irrigation plan. It can take up to several hours to derive useful information from aerial images, and they often do not provide the farmers with substantially new information compared to what they already know [17]. In general, predictive and actionable information with much higher granularity is needed to determine the status of plants and translate them in actionable items that can maximize the crop yield.

In Table 2.3, state of the art water stressed plants detectors are listed. For each of them, advantages and disadvantages are presented. As you can notice, the IR-based sensing, which is going to be exploited during this master thesis, is the best choice between the existing ones.

Method	Advantages	Disadvantages
Soil moisture-based (gravimetry, neutron probes, tensiometers)	Reliable, fast	Labor intensive, destructive Time consuming, highly localized data Deployment of sensors over large areas: energy and cost-prohibitive
Plant-based (leaf-water potential, stomatal conductance, stem and fruit diameter)	Widely accepted benchmark for plant water status Can be very sensitive	Labor intensive, destructive Time consuming, non ok for automation. Highly localized data. Deployment of sensors over large areas: energy and cost-prohibitive
IR-based remote sensing (near IR reflectance, IR thermometry)	Non-contact, sensitive, reliable, fast, non-destructive	Influenced by atmospheric conditions Can cover large areas, but low resolution (satellites) Can cover small areas, but high resolution (IR thermometry) High resolution and large areas is cost and energy-prohibitive
IR-based remote zero-power temperature sensing	Non-contact, sensitive, fine granularity, maintenance-free, real-time monitoring	Other heat sources may trigger false alarms
SWIR-based remote zero-power reflectance sensing	Non-contact, sensitive, reliable, fine granularity, maintenance-free	Requires calibrating for the intensity of impinging sunlight or the use of an external light source

Table 2.3: State of the art water-stress plant detectors

Chapter 3

Methods

To develop the sunlight digitizer idea, briefly explained in Chapter 1 and now discussed in details, three main ideas are explored. These ideas are listed below for completeness of the study:

1. A solar cell which supplies the circuit and works as input for a window comparator.
2. Two normally open switches in parallel, followed by a XOR gate.
3. A normally open switch in series with a normally closed one.

Before starting with the presentation of the three different possibilities, a brief introduction is needed to understand in which sunlight conditions the system should be working. Thinking that the average sunlight irradiance during winter is lower than during summer season, as schematized in Figure 3.1, is straightforward. This comes together with the fact that at noon the irradiance is higher than in the early morning and the afternoon. For this reason, an analysis of the data is performed to find which is the month with the lower average sun radiation. This can be done thanks to the database supplied by the Measurement and Instrumentation Data Center (MIDC) [18]. December comes out to be the chosen month, with an average sun radiation of about $330 \frac{W}{m^2}$ at noon. Intuitively, not every day reaches this value due to a large variety of factors. Then, the chosen value that is going to be used for the whole sunlight digitizer calibration is $220 \frac{W}{m^2}$ because all days go above this threshold. The window of values that will be accepted is 1% of the chosen threshold. In other words, the window within which the system will give a high signal is $220 \div 222 \frac{W}{m^2}$. The window is taken to be 1% because the change of the RWC from 100% to the witting point corresponds to a change in reflectance of about 3.4%. Then, the window cannot be too wide, in order to avoid false alarms

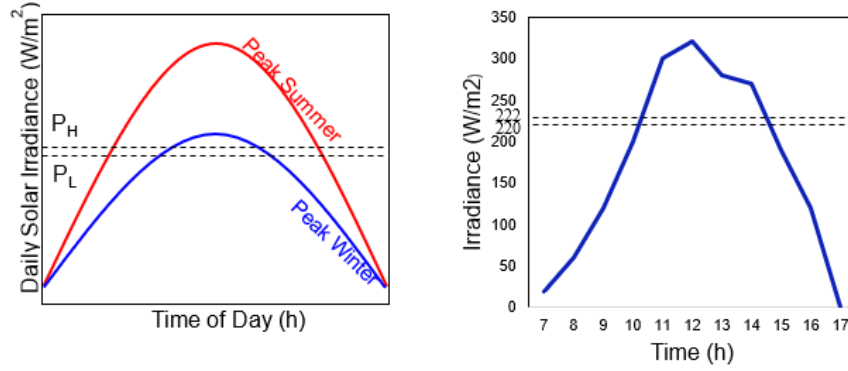


Figure 3.1: Irradiance versus daily hour. Concept on the left and data analysis on the right

(i.e. to avoid that the system works even when it should not). The two values cited above corresponds to threshold powers of respectively 305 and 308 nW . These numbers are obtained with the following formula:

$$P_{th} = K \cdot A \cdot Irradiance_{BB} \quad (3.1)$$

where A is the area of the absorber head ($150 \cdot 150 \mu m^2$), $Irradiance_{BB}$ is the value irradiated by the sun broadband (along all its spectrum), and K is the ratio between the integral of the sun spectrum broadband and the integral of the same spectrum in the specific absorbing area of the reflectance-based sensor (~ 1500 to $1750 nm$, as explained in Section 1.5). The threshold power values are fundamental for the implementation of Option 2 and 3, as in the list at the beginning of this section.

3.1 Option One

Since the goal of such a digitizer is to introduce a working range within which the water-stress sensor is active and remaining always with a low power or, even better, zero power consumption, a solar cell is used to feed all the integrated circuitry in the schematic shown in Figure 3.2. The window comparator, on the other hand, has the role to establish the functioning range, providing as output the so called digitized bit. In this specific case it is represented by the *within* signal, as depicted in Figure 3.3. The *within* signal is high only when the electrical input coming from the solar cell is inside the established working range, as explained below, in Section 3.1.1.

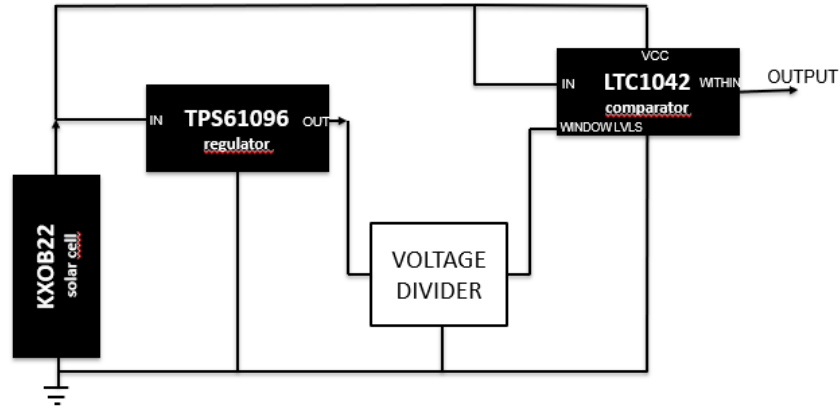


Figure 3.2: Conceptual schematic of the sunlight digitizer

3.1.1 Components

A conceptual picture of the schematic is shown in Figure 3.2, in order to introduce the chosen components. The properties for each of them are explained hereafter. However, a peculiar feature in common between all the components is the extremely low power consumption. To analyze Option One, *LTspice* (high performance SPICE simulation freeware software) has been adopted.

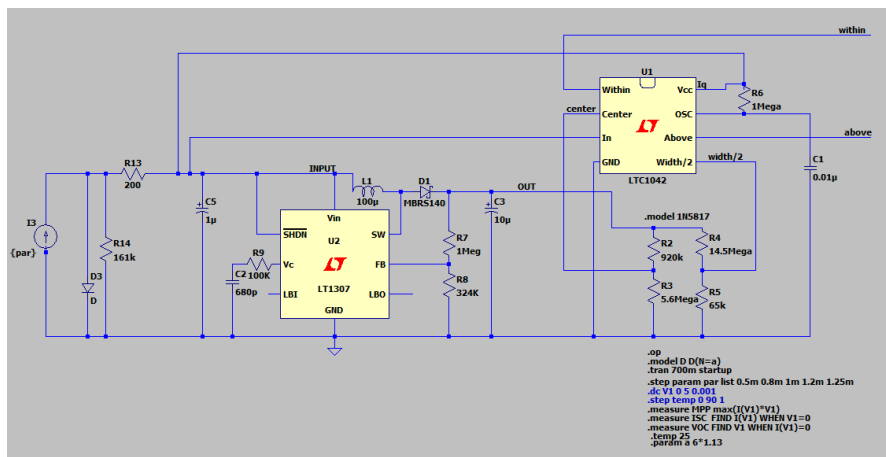


Figure 3.3: LTSpice Schematic for the option 1

Dimensions [mm]	22·7·1.8
Open Circuit Voltage [V]	4.70
Short Circuit Current Density[mA/cm ²]	42.4
Voltage @ mpp [V]	3.40
Current Density @ mpp[mA/cm ²]	37.2
Maximum Peak Power [mW/cm ²]	18.6
Solar Cell Efficiency[%]	22

Table 3.1: Solar cell datasheet features [19]

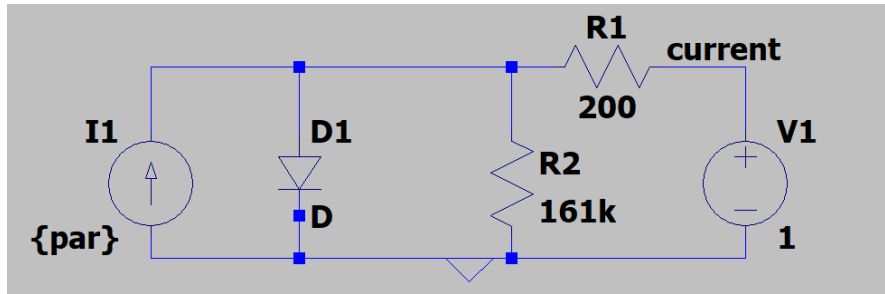


Figure 3.4: Solar cell electrical circuit

Solar Cell

The solar cell by *IXYS* model *KXOB22-01X8F* is selected. In Table 3.1, the main features of this cell are listed. In Figure 3.4, the electrical circuit of the solar cell is presented. The same circuit is present on the left of Figure 3.3. The idea is to reproduce the solar panel in *LTSpice* with the very same characteristics of the datasheet. To do so, the first calculation is the short circuit current I_{SC} , which is given by the following equation:

$$I_{SC} = J_{SC} \cdot A \quad (3.2)$$

where the area A is obtained thanks to the dimensions in Table 3.1, resulting in a I_{SC} of 4.4 mA. As far as the diode is concerned, the forward voltage of a Silicon one usually is around 0.7 V. The solar cell *IXYS 01X8F* is monocrystalline with a spectral sensitivity range that goes from 300 nm to 1100 nm. Then, thanks to its broadband absorption, it can be exploited in indoor as well as in outdoor applications [19]. Due to the much lower percentage of impurities with respect to polycrystalline cells, monocrystalline ones can achieve higher efficiencies, like in this

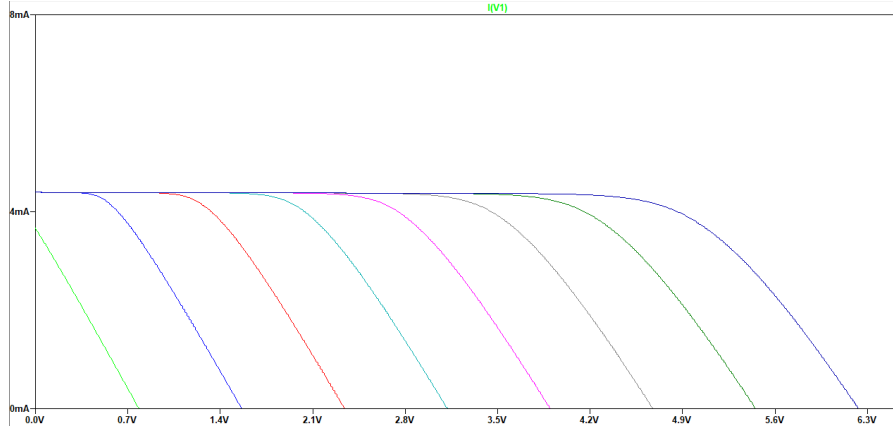


Figure 3.5: Sweep to determine Number of Diodes - SC current versus OC voltage

case, of about 22%. In order to get such an Open Circuit Voltage of $V_{OC} = 4.7 V$ (as in Table 3.1), there is intuitively a need of more diodes in series. Two parameters can be defined in order to achieve a voltage as close as possible to the datasheet value. The first, obviously, is the number of diodes and the second, parameter a in Figure 3.3, is the ideality factor, i.e. how close the model is to an ideal diode. This last value generally varies from 1 to 1.5. There are second order effects that makes the diode not to follow the simple diode equation. For example the ideal diode equation states that the recombination process can occur through band to band or via traps mechanism. However, it can also happen thanks to other mechanisms, like the Auger recombination and the recombination in the depletion region [20]. However, fixing $a = 1.13$ as suggested in [21], and sweeping the number of diodes (parameter N), it is possible to notice that the value that allows to have $V_{OC} = 4.7 V$ is $N = 6$, as in Figure 3.5. Thus, the solar cell model considered contains six diodes in series.

To define shunt and series resistances, the model suggested by Ghani et al. [22] is used. From the I-V curve in the solar cell datasheet, as in the left plot of Figure 3.6, the derivatives in $V = 0 V$ and $I = 0 mA$ is calculated according to the following formulas:

$$\left(\frac{dI}{dV}\right)_{V=0} = -\frac{1}{R_{SH}} \quad \left(\frac{dI}{dV}\right)_{V=V_{OC}} = -\frac{1}{R_S} \quad (3.3)$$

From the calculations of Equation 3.3, the results for the resistances are:

$$\begin{aligned} R_{SH} &= 161 \text{ k}\Omega \\ R_S &= 200 \text{ }\Omega \end{aligned} \quad (3.4)$$

In Figure 3.6, a comparison between the I-V curve of the datasheet, on the left, and of the developed model, on the right, is shown. Furthermore, also the Irradiance-

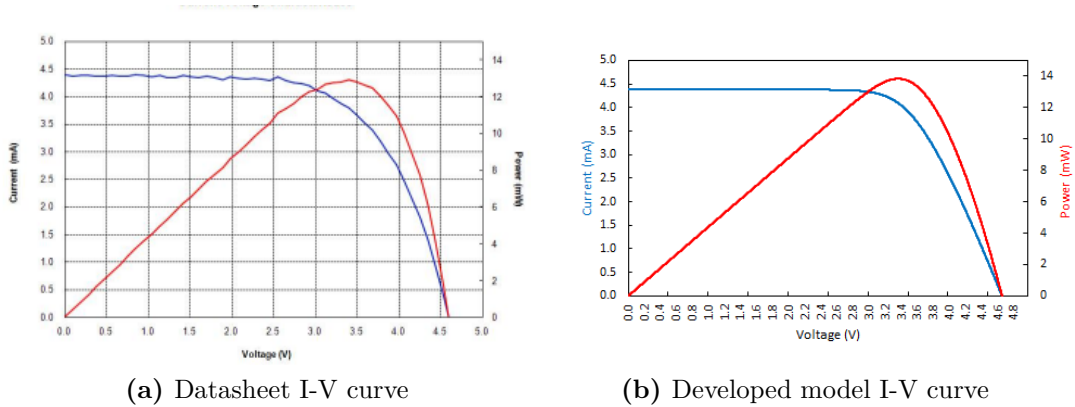


Figure 3.6: Comparison between datasheet curve and my solar cell model

Voltage curve represented in Figure 3.7 is very important to understand which voltage the solar cell is able to provide in the sun conditions set in Chapter 1. According to the collected data, the open circuit voltage that the cell provides is around 3.4 V at $220 \text{ W}/\text{m}^2$. At the same time, it is fundamental to know the current the cell generates at the very same irradiance conditions. In Figure 3.8 this value is presented, obtained by simply doing a step simulation in *LTSpice* and varying the current. As it is possible to see in Figure 3.8, the current I for each

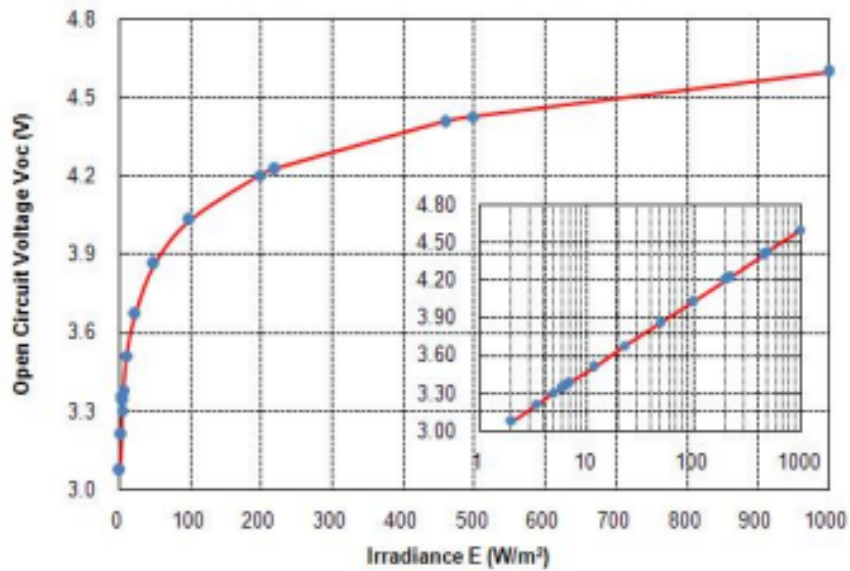


Figure 3.7: Irradiance-Voltage curve of the solar cell

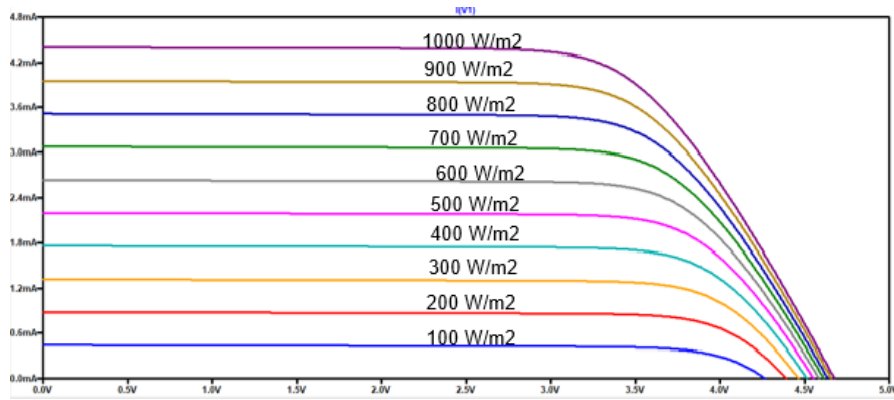


Figure 3.8: Irradiance-Current curve of the solar cell [21] vs Open Circuit voltage

irradiance value is obtained thanks to the following formula:

$$I = I_{SC} \cdot \frac{G}{G_R} = 0.968 \text{ mA} \quad (3.5)$$

where I_{SC} is 4.4 mA at maximum sunlight and the maximum sunlight G_R is 1000 W/m^2 for convention. Then, at a value of G of about 220 W/m^2 , the current is 0.968 mA . It is straightforward to notice the linear proportion between current and irradiance. In order to have an eventually complete solar cell electrical circuit a last step needs to be accomplished, as explained in depth in [23]. It is not sufficient to measure the open circuit voltage only by using a voltmeter (simulated in *LTSpice* with an ideal voltage source) because this can lead to major errors. What we want to measure is the current generated at different irradiance values. In other words, the solar cell is considered as a current generator, not as a voltage source. The method suggested by Chuck Wright involves the following steps:

1. Estimate the current generated at the desired light condition.
2. Calculate the resistance required to have 3.38 V (value valid only in this case, see Section 3.1.1).
3. Add the resistor where the voltmeter was previously placed.

This procedure is useful to maximize the change in voltage for very little change in current. It is important to notice that for a change of 2 W/m^2 in irradiance, as in the case of the sunlight digitizer window, a change of about 30 mV is observed in the voltage. To fulfill the requirements of Point 2, the value R for the resistor is calculated:

$$R = \frac{V}{I} = \frac{3.38 \text{ V}}{0.968 \text{ mA}} = 3.888 \text{ k}\Omega \quad (3.6)$$

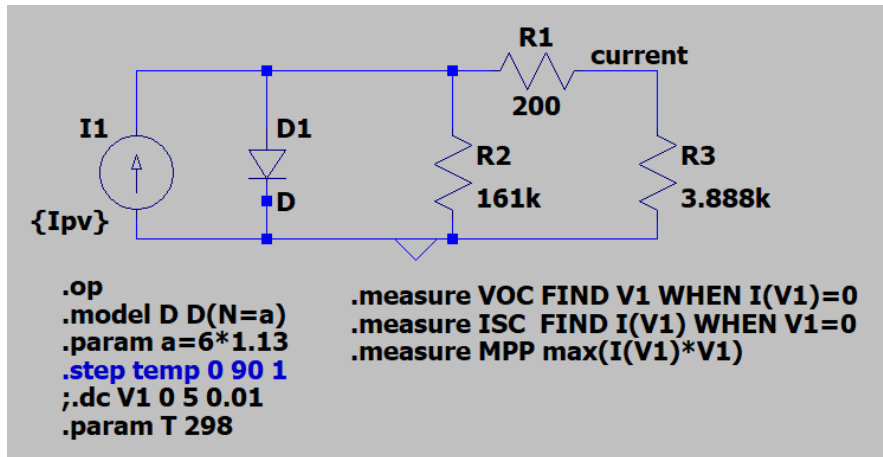


Figure 3.9: Solar Cell Complete Schematic

where V is the voltage that the cell provides at 220 W/m^2 and I is calculated in Equation 3.5. The final electrical circuit for the solar cell is depicted in Figure 3.9.

Step-Up Voltage Regulator

A voltage regulator is necessary for this master project in order to give a constant supply source to both the window comparator and the voltage divider, which aims are explained below in Section 3.1.1, Subsection Window Comparator. The *center* and *width/2* signals need constant voltage to provide a window which remains constant during time. Moreover, to supply the comparator itself, a constant source means a better working of the IC component.

As can be seen in the general schematic presented before in Figure 3.3, the step-up voltage regulator exploited in the schematic is by *Linear Technology*, model *LT1307* (Single Cell Micropower 600 kHz PWM DC/DC Converters). As a matter of fact, the regulators that are going to be tested are both the models *LT1307* and *TPS61096* by *Texas Instruments*. This last component is not simulated in *LTSpice* and it is not present in the schematic since it can not be found in the libraries. However, the characteristics of both components are similar, if not for the fact that the *TPS61096* is even less power hungry than the *LT1307*. Their main features are summarized in Table 3.2.

Then, to make the voltage regulator to achieve a 5 V output, two resistances R_1 , of values $1 \text{ M}\Omega$, and R_2 , of value $324 \text{ k}\Omega$, are put in series at pin number 2 of the *LT1307* component [25]. This is because pin number 2 is the FeedBack (FB) pin and, for this reason, it always provides 1.22 V. According to the following formula,

	TPS61096	LT1307
Dimensions [mm]	3.2	4.9.3
Input Voltage [V]	1.8 ÷ 4.5	1 ÷ 12
Output Voltage [V]	4.5 ÷ 28	1.22 ÷ 30
Quiescent current [μA]	1	3

Table 3.2: Voltage regulator datasheet features [24]

it is trivial to obtain the resistance values cited above:

$$V_{OUT} = 1.22 \cdot \left(1 + \frac{R_1}{R_2}\right) \quad V \quad (3.7)$$

Using similar values for the two resistances, a similar output of 5 V is obtained using Equation 3.7 with the *TPS61096* component, which has a 1 V feedback. To ensure that the output signal remains constant in the input range of our interest, around 4 V, the resulting output voltage of the simulation is shown in the plot of Figure 3.10.

The capacitors, which can be seen in the general schematic of Figure 3.3, present both on the left and on the right of the regulators, are necessary to reduce the noise and to stabilize the input voltage, minimizing the ripple. The input capacitor minimizes the input voltage ripple, suppresses the input voltage spikes and provides a stable system rail for the device [24]. The output capacitor determines the output

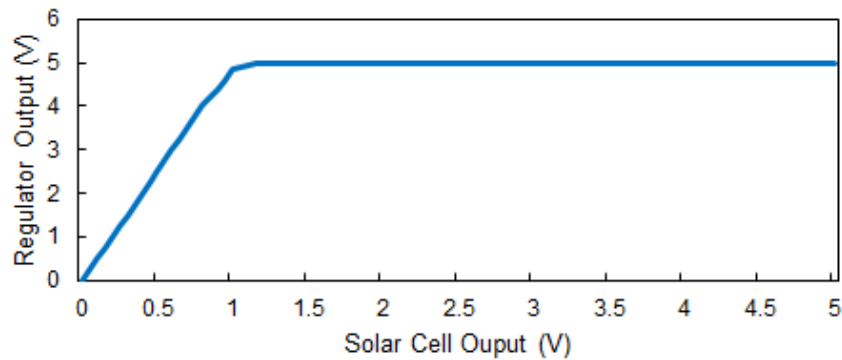


Figure 3.10: Output of the regulator vs output of the solar cell

voltage ripple V_{ripple} according to the following formula:

$$V_{ripple} = \frac{I_{OUT} \cdot t_{delay}}{C_{OUT}} + 0.03 \quad V \quad (3.8)$$

where I_{OUT} is the output current, C_{OUT} is the value of the output capacitor and t_{delay} is typically 10 μs . Although the default hysteresis window of V_{OUT} is 30 mV, due to an internal comparator delay, the higher is the current load the higher is the ripple. Both capacitors are better if made of ceramic and set as close as possible to the regulator pins. Simulations show peaks on both current and voltage in input with a 1 μF input capacitor, but they disappear when a 100 μF one is placed. Obviously, the simulation time is slower when the capacitance is higher. However, velocity is not a constraint in our application.

The V_C pin, as you may see in the general schematic of Figure 3.3, is grounded with a 100 k Ω resistance and a 680 pF capacitor. These are necessary as part of the compensation pin of the error amplifier, as it is clearly shown in Figure 3.11. The LBI and LBO pins, always with reference to Figure 3.3, are useful to detect a low battery input and output, since the typical application for this regulator is to provide a stable output voltage when supplied by a battery. Pin 5, the switch pin, is used to connect the inductor to the diode and pin 3, the shutdown pin, is grounded when we want to disable the regulator and set to V_{IN} or higher when we want the regulator to be in function.

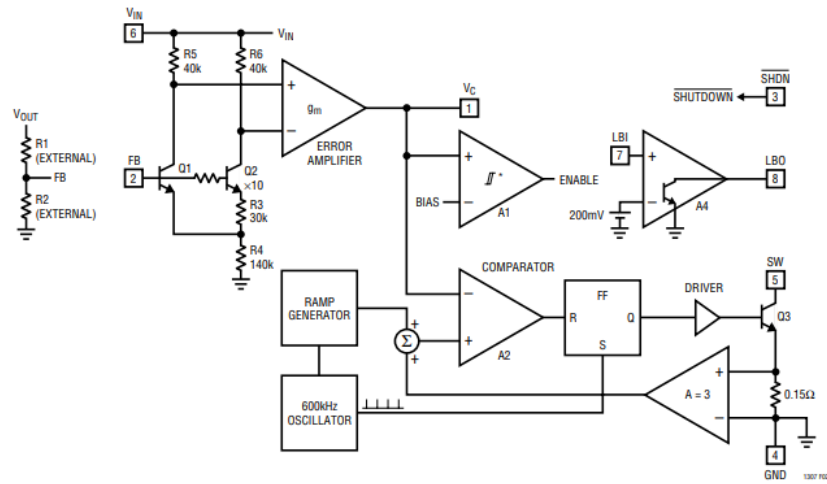


Figure 3.11: Regulator analog circuit

	Output Voltage [V]
Irrad @ 220 W/m^2	3.365
Irrad @ 222 W/m^2	3.395

Table 3.3: Output of the solar cell at the desired irradiance

Dimensions [mm]	10.2·6.5
Supply Voltage [V]	2.8 ÷ 16
Input Voltage [V]	V_{supply} to GND
Quiescent current [nA]	1
Current when ON [mA]	1.2
Response Time [μ s]	80

Table 3.4: Window comparator datasheet features [26]

Window Comparator

The aim of the window comparator is to provide a high signal only when the *output* of the solar cell is within a predetermined window. The circuit inherent to this part is on the top right of the schematic of Figure 3.3. The simulation results at irradiance of 220 and 222 W/m^2 , values obtained and explained at the beginning of Chapter 3, are displayed in Table 3.3. It is now possible to determine a *center* signal (pin 3) which should be the middle point of the values depicted in Table 3.3, i.e. 3.380 V. As far as the *width* signal (Pin 5) is concerned, which is the amplitude of the window, it is trivially calculated by subtracting the two voltage values obtained at the two different irradiance values. The result is 30 mV.

For the window comparator, the chosen component is the *LTC1042* by *Linear Technology*. It exploits the *LTCMOS* silicon gate process technology. The main goal of the OPEN project is to maintain the whole system zero power consumption and, when this is not possible, ultra low power. That is why also this IC is selected to have a very low quiescent current, hence it is defined as a micro-power element. Its specifications are illustrated in Table 3.4. The response time is the result of the sampling cycle: applying power to both comparators, sampling the inputs, storing the results in CMOS output latches and turning the power off. This whole process takes approximately 80 μ s [26]. Thanks to these data it is straightforward to demonstrate the low power consumption of the comparator when the sampling

frequency is 1 *sample/s*, as in the following equation:

$$Power = V_{supply} \cdot I_{ON-avg} = 5V \cdot 1.2mA \cdot \frac{80\mu s}{s} = 0.48 \mu W \quad (3.9)$$

where V_{supply} is the supply voltage and I_{ON-avg} is the average current consumption when the component is on. Actually, at very low sampling rates, as for this purpose, the power consumption is led by R_{EXT} , the resistor linked at pin 7 (OSC). In this case the consumption is:

$$Power = \frac{(V_{supply}/2)^2}{R_{EXT}} = \frac{2.5^2 V}{1M\Omega} = 6.25 \mu W \quad (3.10)$$

This is why the resistor placed is as high as the datasheet allows to, i.e. 1 $M\Omega$.

In Figure 3.12, a block diagram of the *LTC1042* is presented. It is composed by two different comparators, whose outputs are both low in the case where V_{IN} satisfies:

$$V_{center} - V_{width/2} \leq V_{IN} \leq V_{center} + V_{width/2} \quad (3.11)$$

Then, thanks to the NAND gate, the *within* signal results high. On the other hand, the *above* signal is high only when the output of the lower comparator is high, when V_{IN} satisfies:

$$V_{IN} \geq V_{center} + V_{width/2} \quad (3.12)$$

On pin 7 (OSC), a resistor and a capacitance are positioned, as depicted on the top right of the general schematic of Figure 3.3. They are necessary because

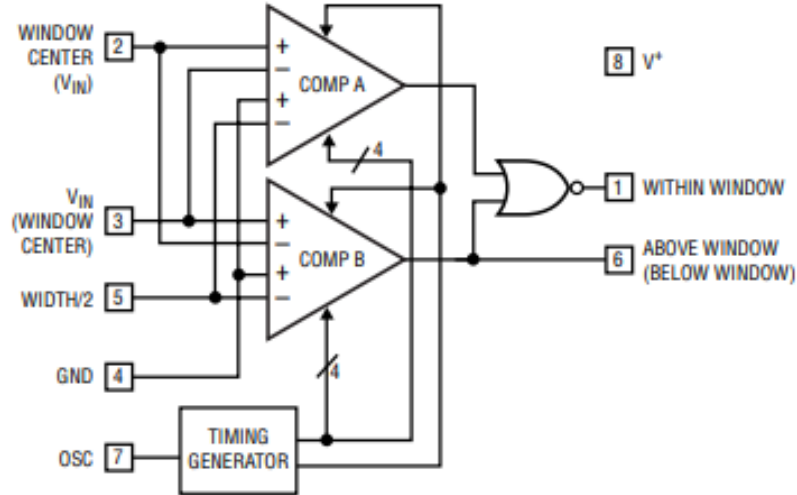


Figure 3.12: Comparator block diagram

R_2	4.25 M Ω
R_3	10 M Ω
R_4	30 M Ω
R_5	50 k Ω

Table 3.5: Values of resistor of the voltage divider

the comparator contains an internal oscillator to strobe itself. The frequency of the oscillation is established by the RC value. The project application does not require high frequency, that is why both passive components have high values of, respectively, 1 M Ω and 0.1 μF , in order to achieve an oscillation of about 5 Hz [26]. Moreover, the group of four resistors R_2 to R_5 on the right of the schematic in Figure 3.3 is the voltage divider. Its function is to reduce the output of the voltage regulator, which is 5 V, to 3.38 V and 20 mV, necessary for, respectively, the *center* and *width/2* signals. The following formulas are adopted:

$$V_{center} = V_{OUT-reg} \cdot \frac{R_3}{R_3 + R_2} \quad (3.13)$$

$$V_{width/2} = V_{OUT-reg} \cdot \frac{R_5}{R_5 + R_4}$$

Since $V_{OUT-reg}$, V_{center} and $V_{width/2}$ are known, only a resistor for each branch needs to be predefined while the others can be calculated out with the formulas of Equation 3.13. This leads to the resistor values reported in Table 3.5. The decision to adopt such big resistors is clearly due to the need to reduce the current flowing through them. The current coming out of the solar cell is about 1.8 mA and the

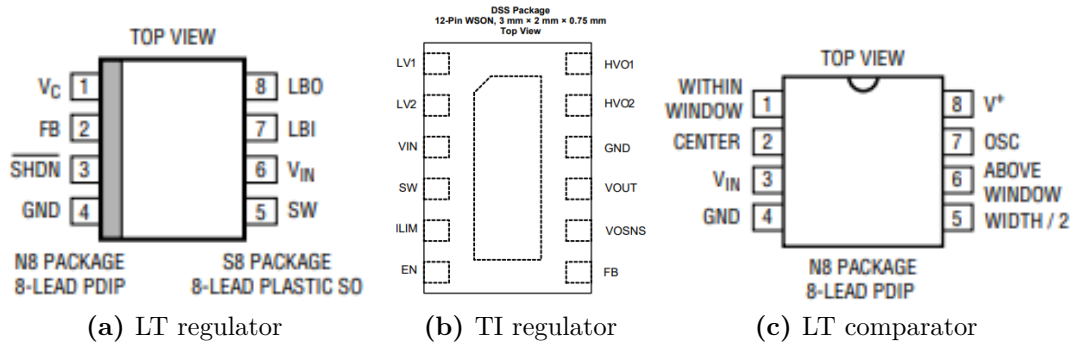


Figure 3.13: Components packages

current absorbed by the regulator is $50 \mu A$. Consequently, the amount of current flowing through the voltage divider, which is the same as the output current of the regulator, needs to be smaller than the input one for a correct working of the circuit. This leads to a drawn current flowing in the divider of $566 nA$, which fulfills our requirements.

In Figure 3.13, the packages of the two regulators (a, b) and the comparator (c) are shown, to better understand the positioning of each pin described above.

3.1.2 Simulations Results

The aim of this subsection is to show the simulation results obtained with the setup deeply explained previously. As in Figure 3.3, a transient analysis with *LTSpice* is performed. The output of the window comparator with the irradiance sweeping from 0 to $1000 W/m^2$ is shown in Figure 3.14. From the results, it can be noticed that the window is not exactly 1% as established, but around 2%. This is due to the noise caused by the output signal of the solar cell and by the output signal of the regulator. It might also be caused by the rumor occurring in the *width* signal since it is supposed to be about $20 mV$, a very small value. In both signals, few capacitors are present. However, bigger capacitors are not simulated on purpose, because they may cause a slower response and the output may not be high when the irradiance is in the predefined window. For this reasons, capacitors of values around units of μF are placed.

Furthermore, the analysis of the currents is performed. As stated in the datasheet, the quiescent current of the regulator *LT1307* is $50 \mu A$ and the one of the regulator *TPS61096* is $1 \mu A$. For the window comparator *LTC1042*, the datasheet ensures a quiescent power equal to $1.5 \mu W$, which corresponds to a $0.3 \mu A$ quiescent current with a V_{supply} equal to $5 V$ [24, 26, 25]. The same currents for the regulator *LT1307* and for the comparator *LTC1042* are obtained from the simulations and they are

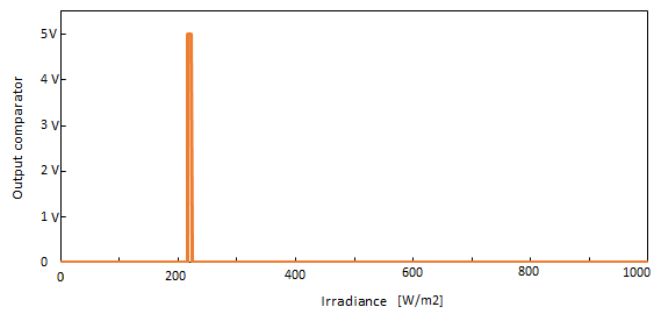


Figure 3.14: Output of the comparator vs irradiance

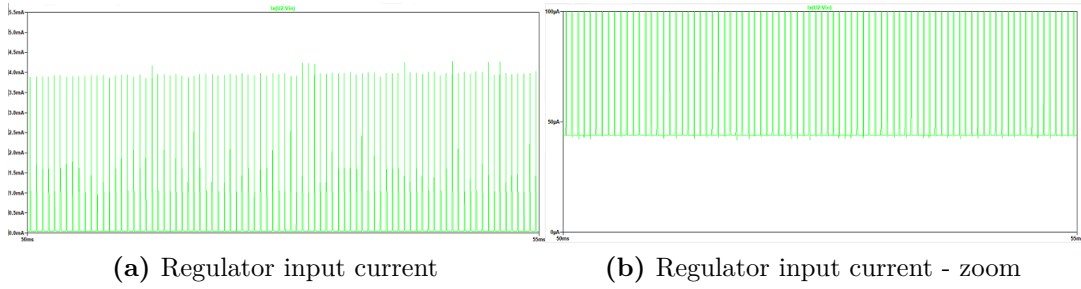


Figure 3.15: Input current of the *LT1307* voltage regulator versus time

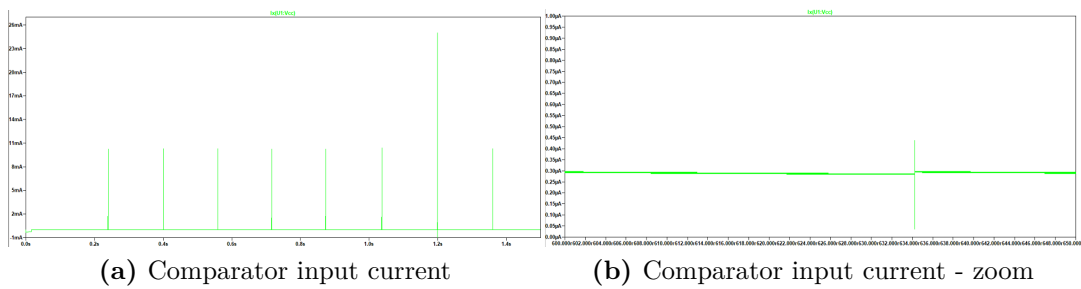


Figure 3.16: Input current of the *LTC1042* window comparator versus time

	Datasheet	Simulation
<i>LT1307</i> regulator	200 μW	172 μW
<i>LTC1042</i> comparator	1.5 μW	1.5 μW

Table 3.6: Comparison of quiescent currents between datasheet and simulations

shown in Figure 3.15 and 3.16, respectively. In Table 3.6, the quiescent currents obtained through simulations are compared with the ones provided by the datasheet. They match and the values confirm the low power feature of both components.

3.1.3 Breadboard Testing Results

As soon as the simulation results shows satisfying results, the testing phase starts. Here below, a list of all the components used in the simulations and then purchased is shown. The circuit with the regulator *LT1307*, used in the simulations, which is called Circuit 1 from now on, is composed by:

1. A solar cell by *IXYS*, model *01X8F*.

2. A $10\ \mu F$ capacitor by *Nichicon*, connected to the input pin of the regulator (pin 6).
3. the regulator *LT1307* by *Linear Technology*.
4. A $100\ k\Omega$ resistor by *Vishay* and a $680\ pF$ capacitor by *Vishay*, connected to the compensation pin (pin 1).
5. A $100\ \mu H$ inductor by *Bourns* between the input pin and the switch pin (pin 6 and 5, respectively).
6. A diode by *Vichay*, between the switch pin (pin 5) and a $1\ M\Omega$ resistor.
7. A $1\ M\Omega$ and a $324\ k\Omega$ resistors connected in series with an edge connected to the feedback pin (pin 2) and the other ones respectively linked with the diode and the ground.
8. A $1\ \mu F$ capacitor by *Vichicon* connected to the diode and the ground.
9. A voltage divider, branch 1, composed by two resistors and a potentiometer: the $4\ M\Omega$ is between the output of the regulator and the center pin of the comparator (pin 2), the $10\ M\Omega$, on the other hand, is linked between the output of the regulator and the potentiometer. This last one is then connected to ground.
10. A voltage divider, branch 2, composed by two resistors and a potentiometer: the $30\ M\Omega$ is between the output of the regulator and the *width/2* pin of the comparator (pin 5), the $50\ k\Omega$, on the other hand, is linked between the output of the regulator and ground.
11. The comparator *LTC1042* by *Linear Technology* is then placed;
12. A $1\ M\Omega$ resistor by *Vishay* connected between the supply pin of the comparator (pin 8) and the oscillator pin of the same component (pin 7).
13. A $0.1\ \mu F$ capacitor linked between pin 7 and ground.

The whole system is shown in Figure 3.17.

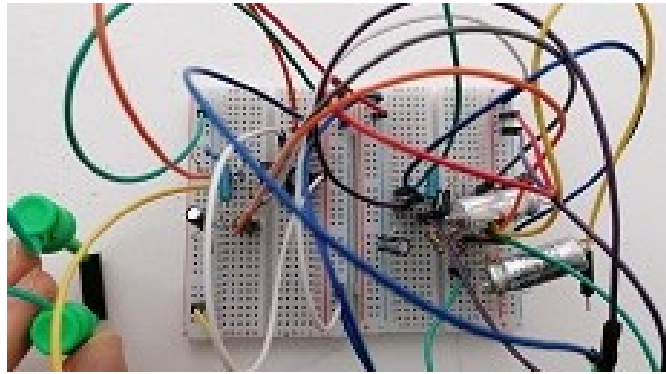


Figure 3.17: Picture of Circuit 1

At the same time, another circuit, which is not simulated on *LTSpice*, is built with a different voltage regulator, *TPS61096*, which is less power hungry. It is named Circuit 2 and its components are listed below:

1. A solar cell by *IXYS*, model *01X8F*.
2. A $4.7\mu F$ capacitor by *MuRata*, connected to input pin of the regulator (pin 3).
3. A $10\mu F$ capacitor by *MuRata*, connected to output pin of the regulator (pin 9).
4. The regulator *TPS61096* by *Texas Instruments*.
5. A $2.2\mu H$ inductor by *Würth* between the input pin and the switch pin (pin 3 and 4).
6. A $10k\Omega$ and a $169k\Omega$ resistors connected in series with an edge connected to the feedback pin (pin 7) and the other ones respectively linked with the diode and the ground.
7. A voltage divider, branch 1, composed by two resistors and a potentiometer: the $4M\Omega$ is between the output of the regulator and the center pin of the comparator (pin 2), the $10M\Omega$ is, on the other hand, linked between the output of the regulator and the potentiometer. This last one is then connected to ground.
8. A voltage divider, branch 2, composed by two resistors and a potentiometer: the $30M\Omega$ is between the output of the regulator and the *width/2* pin of

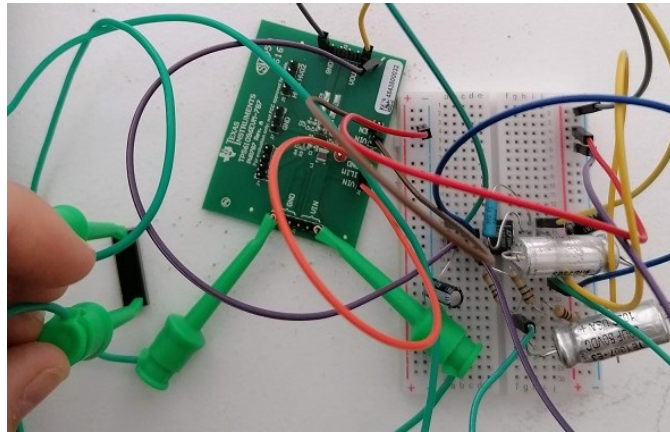


Figure 3.18: Picture of Circuit 2

the comparator (pin 9), the $30\text{ k}\Omega$ is, on the other hand, linked between the output of the regulator and ground.

9. The comparator *LTC1042* by *Linear Technology*.
10. A $1\text{ M}\Omega$ resistor by *Vishay* connected between the supply pin of the comparator (pin 8) and the oscillator pin of the same component (pin 7).
11. A $0.1\text{ }\mu\text{F}$ capacitor linked between pin 7 and ground.

The whole system is shown in Figure 3.18. As explained in the previous subsection,



Figure 3.19: Lights setup



Figure 3.20: Output of the solar cell

the circuit is supposed to work, i.e. provide a high *within* signal, when the irradiance is between 220 and 222 W/m^2 . Obviously, since the testing sessions are performed at home, there is no way to simulate the sun, and it is even more difficult to simulate such a small irradiance range. This is why in this master thesis, a LED and a variable intensity light by *4H-Jena Engineering* with a diffuser are adopted, as in Figure 3.19. The *center* signal needs to be changed in order that the illumination setup described above supplies the solar cell with a different amount of irradiance. The first thing to be tested with this new setup is thus the voltage that the solar cell provides in such conditions. This turns out to be around 4.4 V, as shown in Figure 3.20. Then, changing a resistor in the first branch of the voltage divider and thanks to the use of a 500 $k\Omega$ adjustable resistor by *Bourns*, the *center* signal is adapted to the new sunlight conditions. In Figure 3.21, the *within* signal is displayed. At the same time, changing the intensity of the variable light lamp



Figure 3.21: Within signal high

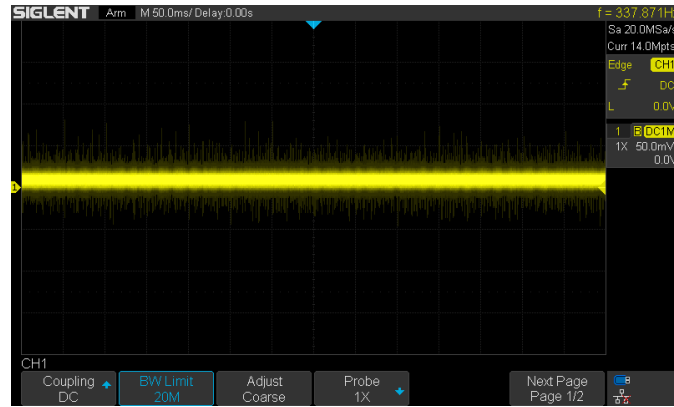


Figure 3.22: Noise of the *width* signal

leads to a *within* signal low and an *above* signal either low or high, when this new illumination setup is respectively below or above the window established by the *center* and the *width* signals.

This latter voltage value deserves a small dissertation on the side. Theoretically speaking, it is expected to be around 30 mV . However, it is already known from the simulations that, due to the noise of the output of the regulator and of the solar cell, it is not possible to achieve such a small value. This is confirmed also during the testing process, as shown in Figure 3.22. In this plot, the capacitors are already placed in meaningful spots, thus the remaining rumor may be due to thermal noise. It is hopefully removed once the testing will be performed on a Printed Circuit Board (PCB). Anyway, this little issue is not a big deal in the functionality of the sunlight digitizer because the only difference is a window that instead of having a 1% range will have a 3% one, as in Figure 3.23. It is to underline the fact that in the meanwhile the team is thinking about increasing this window in order to have more chances that everyday the range around 220 W/m^2 will be present for more than a few minutes. Moreover, it will allow to repeat the measurements, if needed, and it will provide a longer time for the IR sensor to activate itself.

Furthermore, during the testing process of the breadboard, the quiescent currents are measured to confirm the low power features of these electrical components. To do so, the currents are measured according to the definition given by Chris Glaser in [27], i.e. the IC must be in a no-load and non-switching but enabled condition. To do so, all the components, one at a time, are connected to the sourcemeter model 2450 by *Keithley* in no-load condition, but enabled (i.e. if an enable pin exists, then it is connected to a high logical signal, usually V_{IN}). The quiescent current is then measured through the V_{IN} pin, or V_{CC} in the case of the window comparator. For the *TPS61096* regulator, it is not possible to measure the quiescent current in such a way, since an evaluation module already containing the inductor and

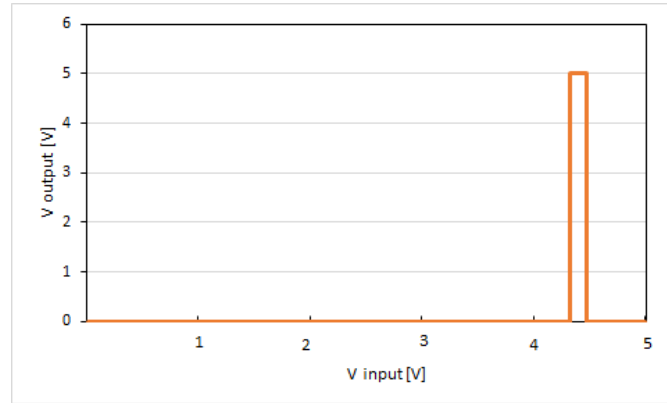


Figure 3.23: Voltage window of the comparator during the breadboard testing

	Datasheet	Simulation	Breadboard Testing
<i>LT1307</i> regulator	200 μW	172 μW	196 μW
<i>TPS61096</i> regulator	4.8 μW	-	20 μW
<i>LTC1042</i> comparator	1.5 μW	1.5 μW	5 μW

Table 3.7: Comparison of stand-by power consumption between datasheet, simulations and testing

the capacitor is purchased. Later on, the stand-by current is measured properly, using a PCB. The values contained in Table 3.7 are the quiescent current values of the evaluation module containing also capacitors and inductors, not removable. That is why the value for the *TPS61096* regulator is bigger than expected. The inductor draw current to maintain a 18 V output, no matter what the input voltage is (provided that it is between 1.8 V and 5.5 V). Also the comparator is showing a value higher than expected. This is due to the resistance placed outside the supply pin, as in Equation 3.10. Increasing that resistance means a reduced power consumption, but corresponds to a lower sampling frequency. Since the value of irradiance may last few minutes, it is better to keep a reasonable value for this frequency. In Figure 3.23, the final plot for the breadboard testing is shown. The sweep on the V_{IN} is performed simply by turning the knob of a DC supply. The window is around 3%.

3.1.4 PCB Testing Results

Once the breadboard testing results shows a correct working mechanism and the proof of concept is demonstrated, the natural prosecution of the evaluation path of this circuit is the design of the PCBs. They provide shorter paths for the signals, less noise and they are compact, thus easy to be integrated into a smaller package for final applications. To do so, *EasyEDA* free software tool is adopted for the design. In Figure 3.24 the schematic and the 3D view PCB of the *TPS61096* regulator are shown, while in Figure 3.25 the same is reported for the *LTC1042* comparator. Two different boards are designed and then tested, one for the regulator and one for the comparator. The choice of having two PCBs is for the sake of simplicity during the testing process and to allow the possibly to use them for different applications. If a part of a component needs to be changed, not the whole printed circuit has to be redone. At this point, the *LT1307* regulator has been abandoned since its excessive power consumption makes the team opting for the *TI* component.

As you can notice from Figures 3.24 and 3.25, in both the schematics more header pins are placed with respect to the necessary ones. This is because in parallel to the analog potentiometers, i.e. adjustable resistors, we want to be certain to be able to achieve any output voltages and any *center* and *width* signals during the testing phase thanks to the digital potentiometer model *AD5165* by *Analog Devices* [28]. In Figure 3.26, the soldered PCBs are shown. The same breadboard testing process is repeated in this context, one PCB at a time. As far as the comparator is concerned, the testing phase has produced good results. As expected, the noise visible in the *width* signal of the breadboard is no longer present, as shown in

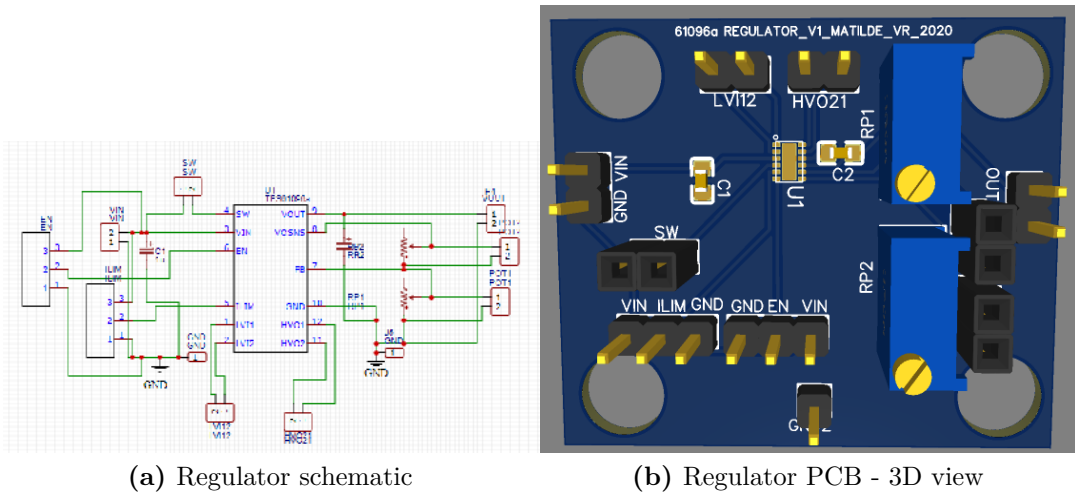
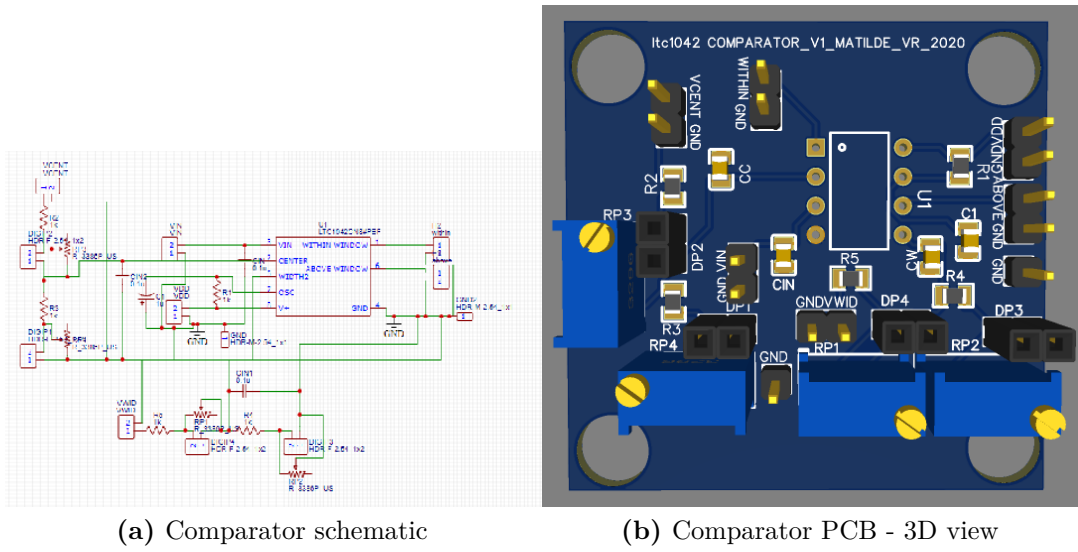


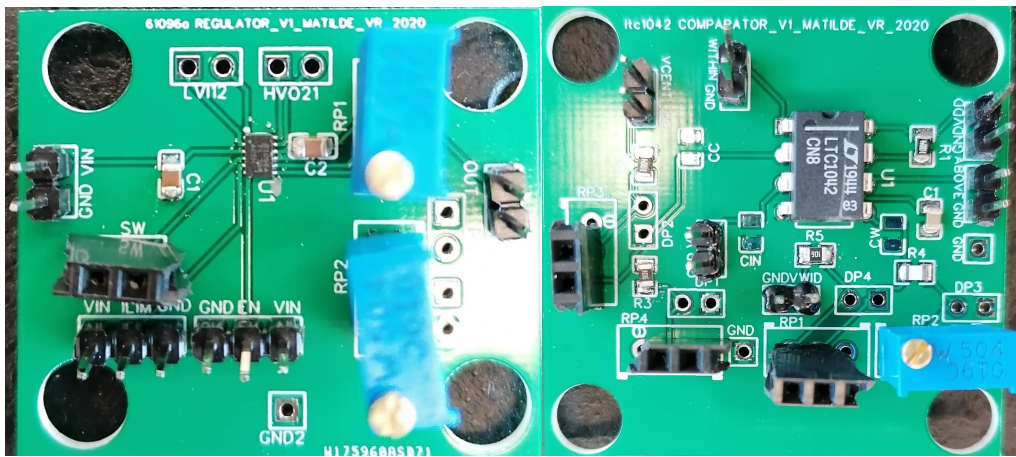
Figure 3.24: *TPS61096* regulator schematic and PCB



(a) Comparator schematic

(b) Comparator PCB - 3D view

Figure 3.25: LTC1042 comparator schematic and PCB



(a) Soldered regulator PCB

(b) Soldered comparator PCB

Figure 3.26: Soldered PCBs

Figure 3.27. Thus, the noise visible in the previous testing phase was probably due to a defective resistor. The *within* and the *above* signals work as expected as well. In this case, the voltage window of the comparator perfectly achieves the 1% requirement, since the *width* signal is able to reach a value as low as 5 mV, without having the noise to overhang it. In Figure 3.28, the 1% window is shown. Also in this case, the sweep of the input voltage is simply obtained by turning the knob of

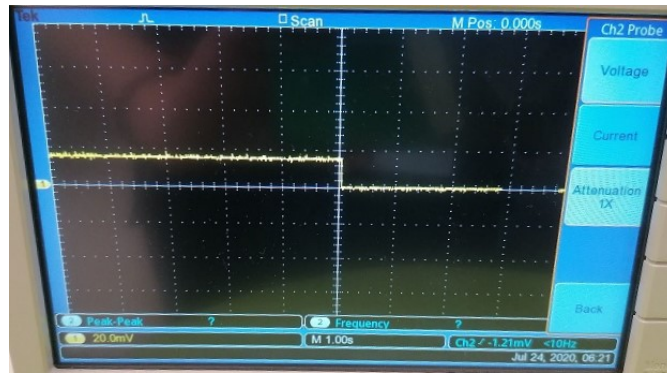


Figure 3.27: *width* signal

a DC supply.

As far as the regulator PCB is concerned, its correct functioning is not verified. The reasons are multiple, the first is because the *TPS61096* IC has dimensions of $2 \cdot 3 \text{ mm}^2$, containing 12 pins. Due to my lack of experience in hot air soldering, I found difficulties during the process, since I was by myself. One related cause is the coronavirus situation in the US and because the accessibility to the laboratory was restricted to few workers at a time. Nobody more expert than me was allowed to help me. Last but not least, I was running out of time. The testing of this last PCB will be the main focus of the project in the coming months. In any case, the *TPS61096* evaluation module tested during the breadboard testing, is used also in this case to show the correct functioning of the whole system: the solar cell plus the two PCBs. The current consumption measurements are performed and shown in Table 3.8. From the *LTC1042* datasheet [26], its power consumption should be around $1.5 \mu\text{W}$, instead of $5 \mu\text{W}$. Like mentioned before, this discrepancy may be due to the R_{EXT} placed at the V_{supply} pin. R_{EXT} currently is $1 \text{ M}\Omega$, but it may go

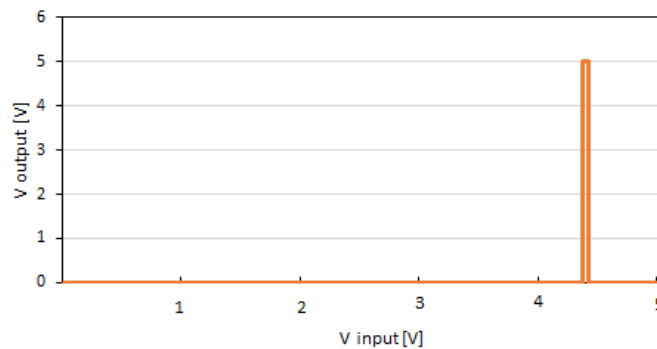


Figure 3.28: Voltage window achieving the 1% window

	Datasheet	Simulation	Breadboard Testing	PCB Testing
<i>LT1307</i> regulator	200 μW	172 μW	196 μW	-
<i>TPS61096</i> regulator	4.8 μW	-	20 μW	-
<i>LTC1042</i> comparator	1.5 μW	1.5 μW	5 μW	5 μW

Table 3.8: Comparison of stand-by power consumption between datasheet, simulations and both testing phases

up to 10 $M\Omega$. Since it is the denominator of the power consumption formula in Equation 3.10, increasing it decreases the consumption itself. In the near future, a new PCB will be soldered with a different R_{EXT} value.

3.2 Option Two

Two normally open devices with different threshold powers are placed in parallel, linked to an ultra low power XOR gate ($I_{cc} \approx 0.5 \mu A$) model *74AUP1G86* by *Nexperia*, as in Figure 3.29. This Option 2 circuit will be called XOR implementation from now on. The advantage of this choice is the simplicity in voltage-based threshold control, allowed by the presence of the two normally open devices. Some disadvantages expected due to the larger footprint, the added hardware complexity and, even if minimal, the power consumption of units of μW . Also in this case

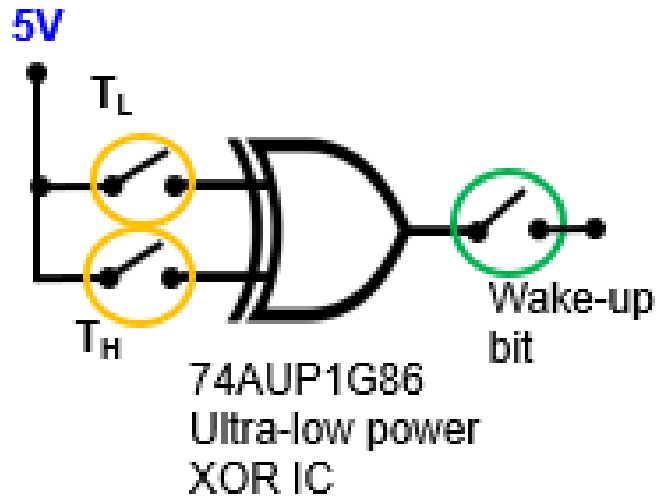


Figure 3.29: Schematic of Option 3

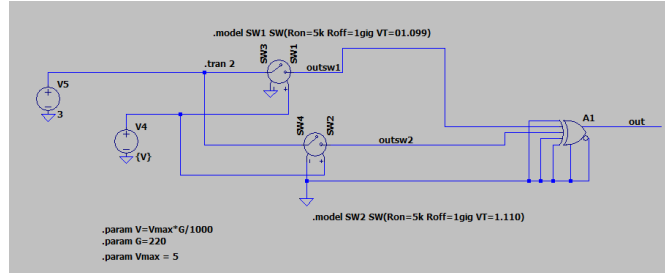


Figure 3.30: *LTSpice* schematic of the XOR implementation

	I_Q [μ A]	V_{CC} [V]	V_{IN} [V]
<i>74AUP1G86</i>	0.9	0.8 ÷ 3.6	Up to V_{CC}
<i>SN74LVC1G86</i>	10	1.8 ÷ 5.5	Up to V_{CC}

Table 3.9: Comparison of the XOR IC used for testing and for simulations

different simulations are performed with *LTSpice*. In Figure 3.30, the schematic of this option is shown. As it is possible to notice, it depicts an ideal implementation since the XOR IC shown has no power consumption, no input voltage range and no input voltage range. In order to achieve a more detailed model the netlist for a real IC component is imported. As in Option 1, the implementation of the parameter list for the *Nexperia 74AUP1G86* is not possible, since it is not available in the *LTSpice* libraries. However, the *SN74LVC1G86* XOR gate by *Texas Instrument* is used, which is very similar to the previous one. The two components features are compared in Table 3.9. As you may notice, both the components can be treated as low power components since it is ~ 10 of μ W in both cases.

The actual schematic with the replaced component is shown in Figure 3.31. On the left of the schematic it is possible to notice the voltage source $V1$ follows a linear relation with the irradiance. The maximum voltage reached at the maximum irradiance (1000 W/m^2) is established to be 5 V . For this reason, the two thresholds for the voltage-controlled switches ($SW1$ and $SW2$) at 220 W/m^2 and at $222, \text{ W/m}^2$ are respectively 1.10 V and 1.11 V . On the very left, another voltage source is placed to make sure that, if the switch is closed, a voltage is present to be detected by the XOR gate as a high signal. The two photoswitches are designed in order to have a resistance when the switch is closed or equal to $5 \text{ k}\Omega$, which is the actual resistance that the current devices provide when active, i.e. when there is a contact. When the switch is open, on the other hand, the photoswitches provide a $1 \text{ M}\Omega$ resistance, i.e. an open circuit. On the right, the model for the XOR implementation is depicted with two inputs, the supply voltage, ground and the

output. In order to maintain also this system as low power as possible, the same solar cell cited in Option 1 is exploited. The output signal is set to high only when one of the two inputs is high and the other is low, i.e. the irradiance is within the predefined range. Contrarily, the output is set to low when either both or none of the photoswitches are closed. The two photoswitches are both closed when the irradiance is too high, i.e. when the reflectivity of the leaf is not reliable since it may be affected from the extremely sunny day. This other situation (both open) arises when the irradiance is too low and hence not inside the range of interest. The correct working system is shown in Figure 3.32.

3.2.1 Simulation Results

The output is correctly high only in the desired range, within the 1% window from $220 W/m^2$ to $222 W/m^2$. This implementation may be straightforward to realize in laboratory. It is sufficient to place two working devices with the same, or at least similar, threshold voltage in the vacuum chamber. Once there, thanks to the electrical connections that the chamber supplies, it is necessary to apply different pull-in voltages such that the threshold voltages are equals to the desired ones. To be sure that this is achieved, it is possible to exploit the heaters under the absorber head as explained in Chapter 1 in order to calculate the threshold power and consequently the minimum voltage necessary to close the contact. In the probable case in which a difference in threshold of only $10 mV$ is not achievable, a lens can be placed above the $ZnSe$ window of the vacuum chamber. Also in this case the same lens used in Chapter 1 can be exploited, using a smaller magnification. This is because already a $50 mV$ threshold difference is easily obtained with the current tools.

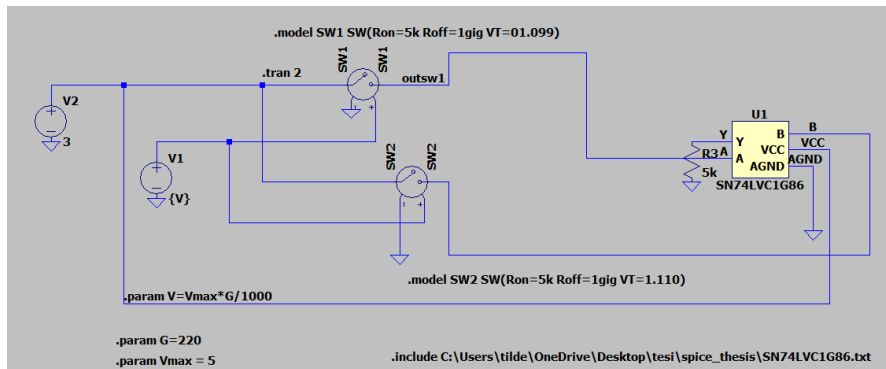


Figure 3.31: *LTSpice* actual schematic for the XOR implementation

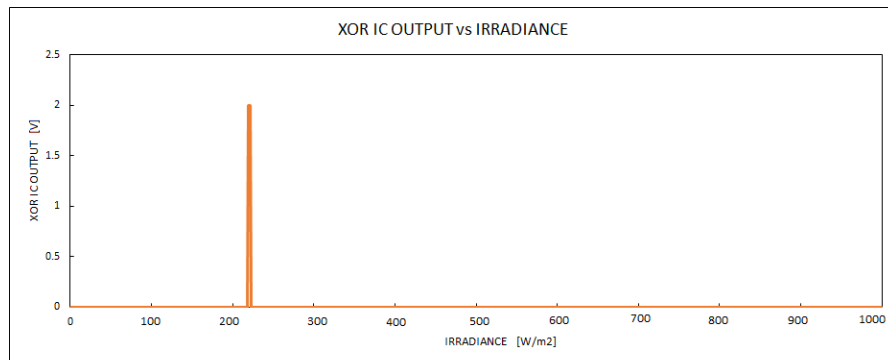


Figure 3.32: *LTSpice* simulation of XOR IC output vs irradiance

3.3 Option Three

A normally closed device (i.e. the contact is closed) is connected in series with a normally open one (i.e. the contact is open), as shown in Figure 3.33. The former is the upper limit detector, which corresponds to the high level of the irradiance window, i.e. 308 nW . It opens when the sun irradiance is greater than the threshold of the normally closed device. The latter corresponds to the lower irradiance limit, i.e. 305 nW , and it closes when the irradiance exceeds this threshold. Both these

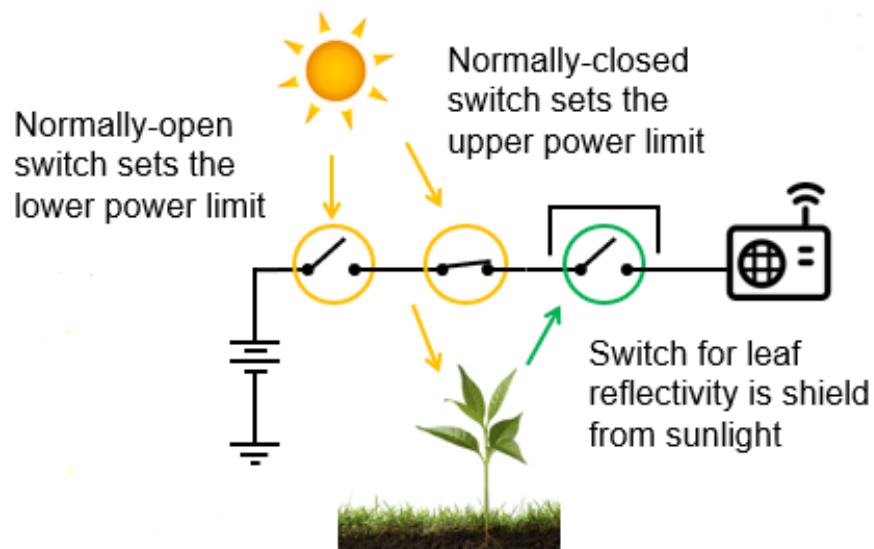


Figure 3.33: Schematic of Option 3

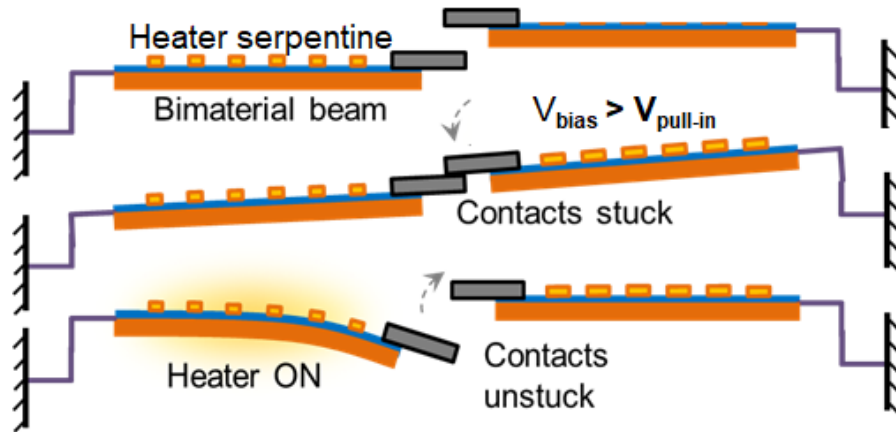


Figure 3.34: Normally closed switches technique

two micromechanical sensors are placed in series with the leaf reflectance detector and the whole effectively checks the leaf reflectance (or temperature) only when both switches of the sunlight digitizer are closed, i.e. when the solar irradiance is within the window. This solution provides zero standby power consumption, low complexity and a minimized footprint since all switches are fabricated on a single die. However, even though the group has observed normally closed devices and has ways to create normally closed devices from normally open devices, the team is still working on ways to control the threshold of normally closed devices. A technique to obtain normally closed switches is based on sticky normally open devices and by using the pull-in voltage method. An observed repeatable reopen threshold of $\sim 1.06 \mu W$ is found thanks to the serpentine heater above the reflector head. The concept is illustrated in Figure 3.34. In Table 3.10, the advantages and the disadvantages for the three options are summarized.

	Pros	Cons
Option 1	battery-less	larger footprint, complexity
Option 2	only NO devices	larger footprint, power units of μW
Option 3	minimized footprint	lack of threshold control in NC devices

Table 3.10: Advantages and disadvantages of the three options

Chapter 4

Conclusions

4.1 Final Results

Throughout this master thesis, the following results have been achieved:

1. A complete electrical solar cell model, as in Figure 4.1, developed to establish with extreme accuracy the output voltage at a certain irradiance value.
2. A fully operational sunlight digitizer tested with the breadboard complete setup as in Figure 4.2, providing a 3% window, and tested with a positive feedback also when supplied with the solar cell, as in Figure 3.23 of Section 3.1.3.
3. A fully operational window comparator PCB with 5 μW power consumption, as in Figure 3.26 of Section 3.1.4. Mechanism tested also when supplied with the solar cell.
4. A fully operational sunlight digitizer composed of the *01X8F* solar cell by *Ixys*, an evaluation module for the voltage regulator *TPS61096* by *TI* and the window comparator model *LTC1042*.
5. As side work, as explained in details in Appendix A, a water pump is connected to the IR sensor, which is described in Chapter 1, and fed uniquely by the IR sensor when activated by a low RWC of a soybean alive plant. All this is achieved with the help of a ultra low power load switch.

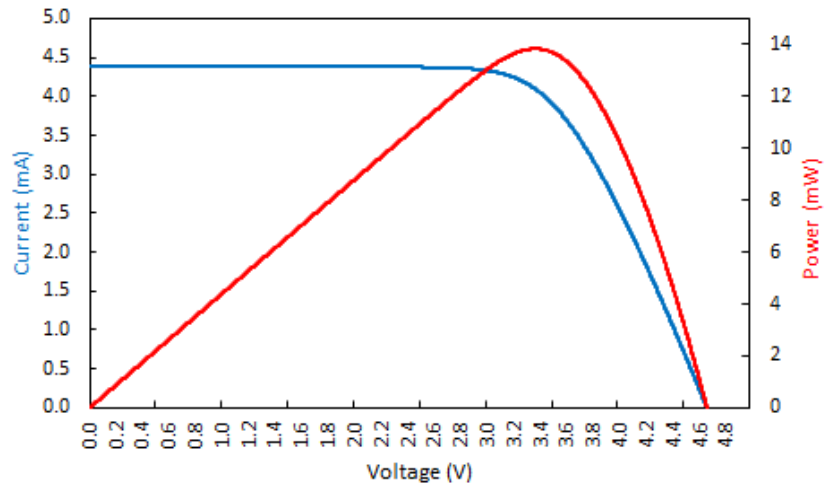


Figure 4.1: I-V curve of the solar cell, results of the *LTSpice* simulation

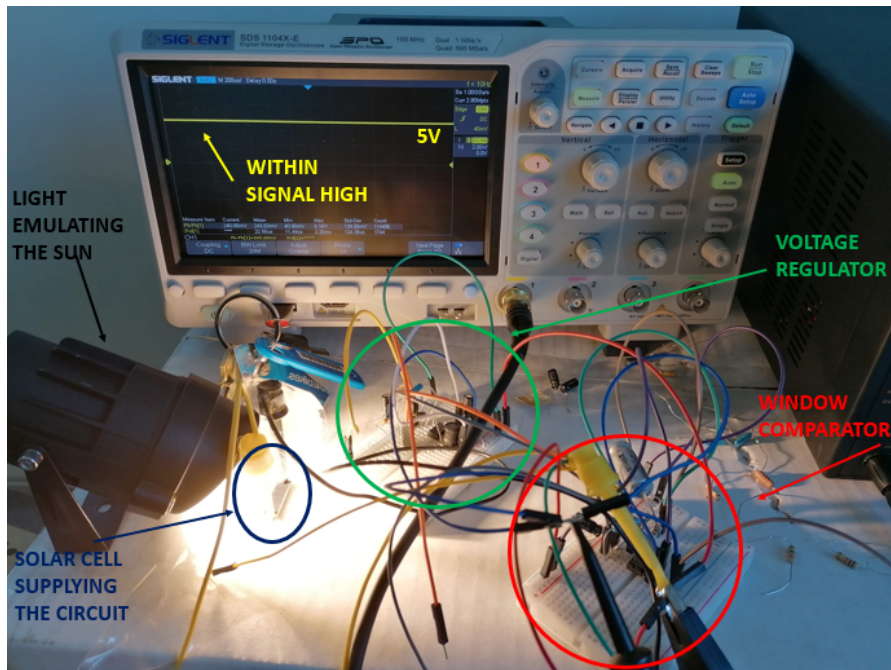


Figure 4.2: Breadboard complete setup

4.2 Next Steps

4.2.1 Packaging

For field testing and deployment, the current setup of testing devices inside bulky vacuum chambers is understandably unfeasible. To mitigate this issue and eventually demonstrate miniaturized sensor nodes for remote deployment, the team is working towards a chip-sized vacuum packaging solution. Vacuum packed devices are already implemented in the old device designs [29]. This proves the compatibility of the current technology with commercial vacuum packaging processes and demonstrate Commercial Out of The Shelf (COTS) electronics interfacing. As part of this project, the plan is to package the new devices on a larger scale and eventually work towards demonstrating a system-level implementation of a network of remotely deployed miniaturized water-stress sensors. The vacuum package features are listed below:

1. Packaged by *INO Inc.* with proprietary low temperature ($\sim 170\text{ }^{\circ}\text{C}$) packaging process.
2. $\sim 15\text{ mm} \times 15\text{ mm}$ chip mounted on Leadless Chip Carrier (LCC) 68 ceramic header.
3. $3 \div 14\text{ }\mu\text{m}$ IR-transparent window.
4. $\leq 3\text{ mTorr}$ vacuum pressure (previous packages are shown to maintain this level even after 3 years [29]).
5. Internal COTS MEMS pirani gauge included to monitor package pressure .
6. ≥ 10 devices wire-bonded per chip for redundancy and improved functionality.

The whole system idea is shown in Figure 4.3. On the left, the IR-activated PMP controls the load-switch, which connects the 3 V battery to the wireless microcontroller [30]. On the right, the PMP is connected to one of the GPIO terminals of the microchip. The timer circuit shares the same power supply of the microchip and, when turned on, it sends a pulse to the heater after a 1 s delay to automatically reset the switch [29].

Appendix A

Side Work - Connection of a Water Pump to the IR sensor

The goal of this side work is to show that our plasmonically-enhanced IR sensor is able to activate a water pump thanks to its output only, without any external input. It may look very simple but our MEMS device alone, for reasons concerning its size, can not flow an amount of current sufficient to feed a pump, i.e. a current of hundreds of mA would burn the whole device. To overcome this obstacle, the conceptual schematic of Figure A.1 is developed. As you can notice, a Load Switch (LS) is part of the schematic. This latter component is essentially an electronic switch that can be used to turn on and off the power supply rails of the systems, similar to a relay or a discrete Field Effect Transistor (FET). Load switches offer many other benefits to the system, for example some protection features that are often difficult to implement with discrete components [31].

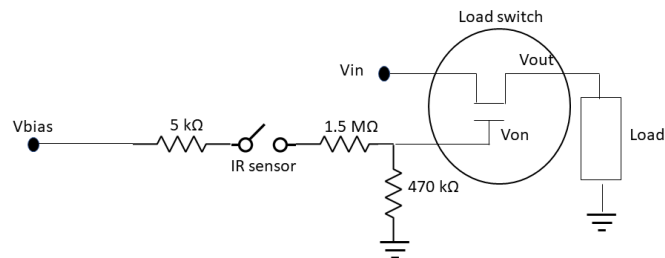


Figure A.1: Conceptual schematic of the system

	<i>TPS22860</i>
V_{bias}	$1.65 \div 5.5 V$
V_{input}	$0 \div V_{bias}$
I_{switch}	$200 mA$
$I_{leak-input}$	$2 nA$
$I_{leak-bias}$	$10 nA$

Table A.1: *TPS22860* datasheet specifications

First of all, it is necessary to identify a load switch which has the characteristic common to the philosophy of this project, i.e. to be ultra low power. For this purpose, the ultra-low leakage load switch model *TPS22860* by *Texas Instruments* is selected [32]. In Table A.1, the main specifications of this switch are cited. The IR sensor is used during these testing process is subject of the research of the pull-in voltage. For this specific IR sensor, the $V_{pull-in}$ turns out to be $20 V$. As it is possible to notice in Table A.1, this pull-in voltage is not a suitable bias voltage for the load switch. For this reason, as you can see on the right of the device in Figure A.1, a voltage divider is used. Since the V_{bias} cannot be higher than $5.5 V$, suitable resistor values are $470 k\Omega$ for the one connected to ground and $1.5 M\Omega$ for the one connected in series with the device. On the other hand, the $5 k\Omega$ resistor, which is placed before the sensor, is present only to represent the on resistance of the sensor itself. The V_{bias} is then obtained thanks to the following formula:

$$V_{ON} = V_{supply} \cdot \frac{470k\Omega}{1M\Omega + 470k\Omega + 5k\Omega} = 4.76 V \quad (A.1)$$

where V_{supply} is the pull-in voltage of the IR sensor. Thus, when the device is active, i.e. there is a plant with an RWC (concept explained in Chapter 3) lower than 65.8% in front of the transparent window of the vacuum chamber where the MEMS is placed, the load switch receives a voltage of $4.76 V$. At this point the LS is closed and allows the V_{input} to be transmitted to the output and reach the load, i.e. the water pump.

At this point, there is another LS specification that needs to be fulfilled: it can support only $200 mA$ flowing while the water pump currently in use works with $600 mA$. This problem is temporarily solved soldering three evaluation module PCBs containing the selected *TPS22860* in parallel, as shown in Figure A.2. In this way, the whole system is able to supply $600 mA$ to the water pump, current that results to be sufficient to make it work properly. In Figure A.3, the complete setup is shown.

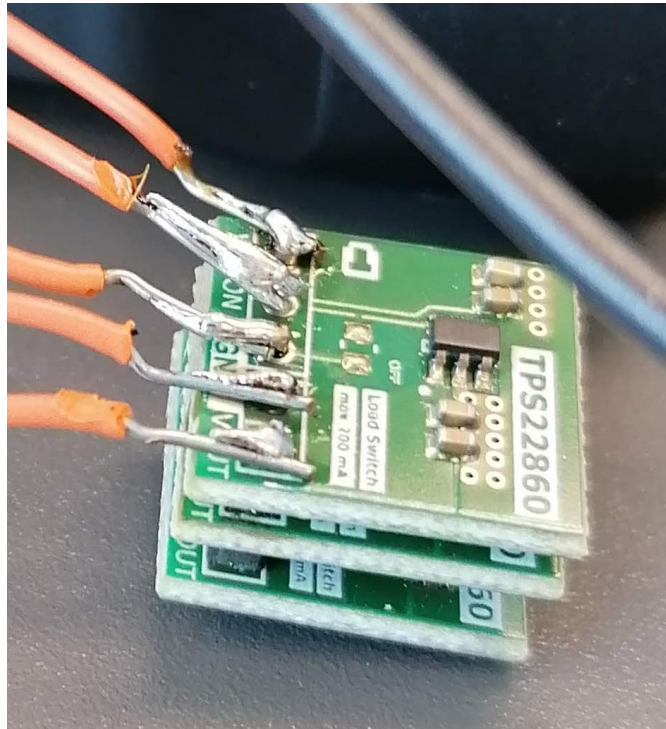


Figure A.2: The three PCBs soldered together

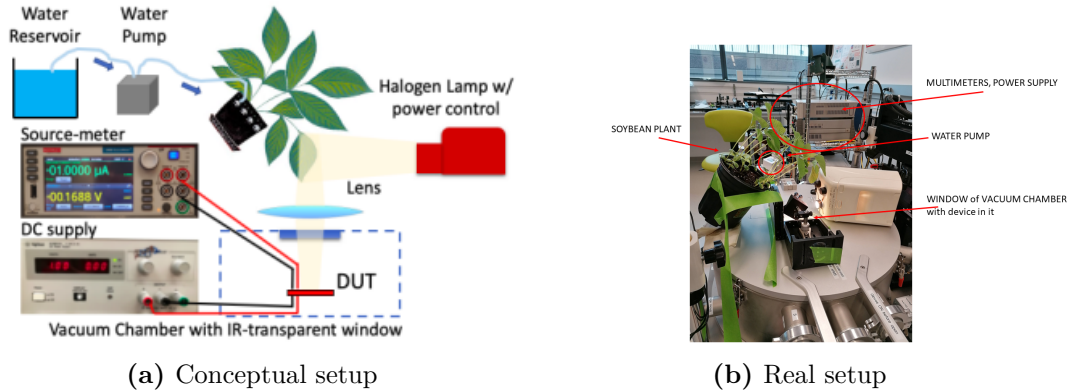


Figure A.3: Conceptual (on the left) and real (on the right) setup

The soybean *Glicine Max* plant is used as always throughout this master thesis. Since the pull-in voltage results to be 20 V as suggested before, in order to make our nanometric device be the cause for the switch to open itself, a bias voltage is applied. This value will change together with the drying process of the plant, i.e. with the decreasing of the RWC of the leaf.

Time of the day [h]	RWC [%]	Bias Voltage [V]
13:50	100	19.8
14:10	91	19.6
14:45	85	19.5
15:25	75	19.2
15:55	68	19
17:00	47	18.5
17:36	25	17

Table A.2: Bias voltage changing with the RWC

To underline once again the almost zero power consumption of this system, it is necessary to highlight that the bias voltage does not make the device consume any power since, when it is applied, no current flows through the device. At the same time, this voltage intuitively decreases together with the decreasing of the RWC since when the leaf dries up, its reflectivity increases, as explained in Chapter 1. Then, one more testing needed is the research of the bias to be applied when the leaf is at around 65%, the lowest percentage from which the plant is able to recover. To do so, the data summarized in Table A.2 is presented. As you can notice, the trend is mostly linear apart from when the leaf is very dry, almost dead. However, these final measurements are not of our concern. Thanks to these values, it is possible to finally define that the bias voltage to be applied at the IR device is 19 V.

Now, to show that the whole setup works properly, a voltage of 19 V is applied. The plant is placed in front of the transparent window containing the device. The sensor turns on due to the reflectance of the leaves, the output sets to high and the pump starts pumping water to the plant. To be sure that it is not working at any plant reflectivity, a 100% RWC soybean plant is placed in front of the vacuum chamber and, with the same bias, the device does not turn on. However, it does turn on when applying an higher bias voltage of around 20 V. Thus, the complete mechanism is proven.

Ultimately, a test of the current consumption is performed on the same setup. The goal is to compare the stand-by current flowing when the pump is connected to the IR device and when it is connected to its own batteries. In both cases there is no load. The results are displayed in Table A.3 and shown in Figure A.4. It is possible to conclude that the water pump linked to the device which is the focus of

Quiescent current - connected to device	Quiescent current - connected to batteries
180 nA	28.4 μ A

Table A.3: Quiescent currents when the pump is connected to the IR device and when it is connected to its own batteries

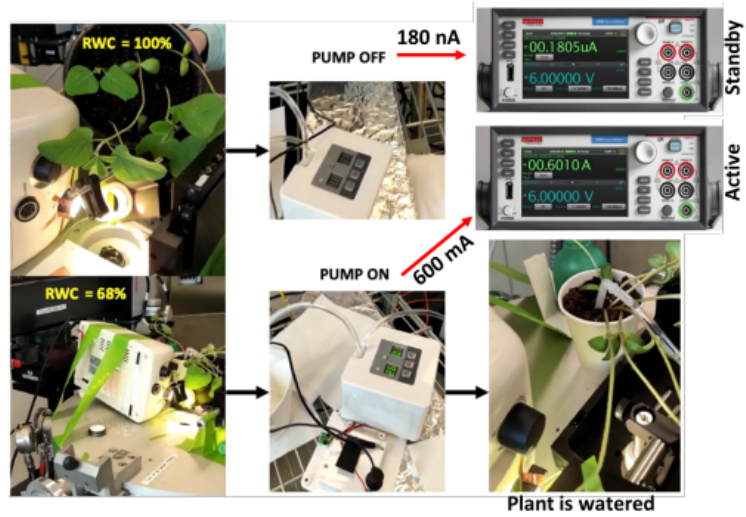


Figure A.4: Current consumption when the pump is OFF and ON

this thesis consumes 160 times less power than when connected to its own batteries. A confirmation that the whole system is carrying on being a very low power sensor. In the future, new tests will use a better load switch IC (*SiP32431*) that has been recently found, capable of much lower standby current ($\sim pA$) and much higher current handling capability ($\sim 1.4 A$).

Appendix B

Paper

During my stay in the NSaNS Laboratory, at Northeastern University, the following paper has been written containing all the last achievements of the group on the IR sensor, applied to crop applications. It is currently in the review phase and it will be submitted to the journal *Nature Electronics* soon.

Zero Power Crop Water-Stress Detector leading to the optimization of water usage and yield

Antea Risso^{1*}, Vageeswar Rajaram¹, Sungho Kang¹, Sila Deniz Caliskan¹, Matilde Maria Pavese¹, Zhenyun Qian^{1,2} and Matteo Rinaldi^{1,2*}

Agricultural sensors are potentially a powerful tool to optimize the crop productivity while conserving natural resources. State-of-the-art soil moisture sensors rely on active-electronics to indirectly measure the plant water-stress thereby being power hungry and inaccurate. Here we report the first short-wavelength infrared (SWIR) micromechanical photo-switch (MP) suitable for the detection of water-stress in leaves with zero-power consumption in standby. This detection mechanism exploits the energy in a specific narrow-spectral band of solar radiation reflected off leaves that is strongly correlated to the water content in plants. Based on bi-material cantilevers, the proposed MP employs a high-efficiency IR plasmonic absorber matched to water's spectral absorption band, to produce a digitized wakeup-bit only when the leaf starts showing an indicator of early-stage water-stress, while remaining dormant with zero power consumption when the leaf is healthy. The results pave the way for the development of high-granularity, maintenance-free sensor networks for large-scale smart farms.

THE agriculture industry currently faces an urgent need to improve the crop productivity in response to the rapidly increasing competition for arable land and exposure to climatic shocks. The population-driven need for food in the world is projected to increase by 70% by 2050, while land and natural resources such as water become scarcer for farming¹. Therefore, increasing the efficiency of food production is incredibly important to avoid global shortages. Genetic studies show that the average yield achieved in commercial farms is only one tenth of the theoretical maximum yield. Farmers make over 40 yield-impacting decisions each season, therefore there is a clear need to develop decision support tools that maximize economic returns². The capability of acquiring comprehensive and real-time data of plant health and environmental conditions, with high granularity, and translating them in actionable items would maximize the crop yield while conserving natural resources.

Optimizing irrigation based on in-field spatiotemporal data reflecting crop water-need is one of the most important actions that can be taken in this regard. Existing state-of-the-art technologies for detecting plant water-stress, however, cannot be used to implement such a continuous monitoring of large-scale crop fields as explained below.

Significant research effort has resulted in the creation of several agritech startups³ who currently offer smart sensors to monitor the water content in the soil and provide simple, actionable and accurate irrigation decisions. Nevertheless, they have been facing the fundamental challenge associated with remotely deployed sensor technologies: standby power consumption. Despite the progress in engineering energy efficient systems, existing sensors typically stop working after few weeks in the ground because running out of battery power⁴. Some sensors employ a solar panel for power to increase

deployment time. However, this increases the sensor cost, complexity and size due to inclusion of the solar cell, its associated electronics and rechargeable batteries. Thus, it is unfeasible to greatly scale such sensors (in both spatial granularity and deployment area) owing to high initial investment and maintenance costs.

Soil moisture sensors are used intensively at present because it gives real time readings. Tensiometers are already used in irrigation scheduling but the soil moisture tension strongly depends on the type of soil as well as periodic maintenance is required due to the accumulation of air bubbles over time. Granular Matrix Sensors (GMS) are cheaper and require less maintenance but they show different responses to different soil types too and they are less accurate in sandy soils. Time Domain Reflectometers (TDRs) have a very quick response to soil moisture changes but they are costly and have low accuracy when there's high clay content and elevated levels of salinity in the soil. Unlike TDRs, Frequency Domain Reflectometers (FDRs) can be used with soils having high salinity but it requires soil specific calibration^{5,6}.

Satellite-based hyperspectral infrared (IR) imaging is typically used to monitor large areas at once but this approach is characterized by severely limited spatial and temporal resolutions (~weeks). Most recently, thermal or hyperspectral infrared cameras combined with unmanned aerial vehicles (drones) have been employed for imaging large area of crop field from the air.

Nevertheless, the costs involved with this approach are prohibitive for frequent inspections throughout the production cycle. Moreover, further data processing and interpretation by experts are required to make decisions on the most effective irrigation plan. It can take up to several hours to derive useful information from aerial images, and they often do not provide the farmers with substantially new information compared to what they already know⁴.

¹Department of Electrical and Computer Engineering Northeastern University, Boston, MA 02115 USA. ²Northeaster SMART Center, Boston MA 02115 USA. *e-mail: risso.a@northeastern.edu, rinaldi@northeastern.edu.

ARTICLE

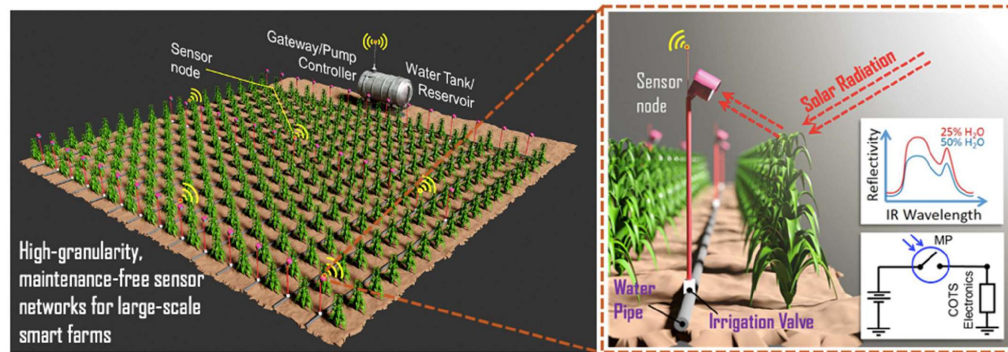
nature
electronics

Figure 1. **a**, Schematic illustration of the proposed zero-power and low-cost nodes deployed in the field: SMART Farm. **b**, Schematic of the MP used for non-contact water stress detection in plants. Upon plant water-stress detection, the switch closes and connects the battery to any active electronic function e.g. a wireless transmitter that remotely triggers an automated irrigation system. The switch remains otherwise OFF with zero drain on the battery. **c**, Water-stress related IR characteristic of plants (i.e. leaf reflectivity) in the crop field. The sun light reflectivity of the leaf increases when the relative water content of the leaf (RWC) decreases. **d**, Simplified schematic of the circuit showing the MP in between the battery and the COTS electronics.

On the other hand, IR-based water content monitoring techniques are particularly attractive since they are non-destructive and can be completely automated requiring lesser complexity in measurement and data processing to accurately determine plant stress. Current IR-based methods use handheld devices (thermal and hyperspectral cameras), which are bulky, labor intensive (requiring advanced operator training) and extremely costly.

Driven by the growing need for a solution that detects crop water stress over large areas with high spatial and temporal resolution while being cost, labor and energy-efficient, significant effort has been recently devoted to creating completely-passive zero standby power sensors capable of detecting, distinguishing and digitizing the signal of interests without using active electronics⁷⁻⁸.

In this article we present a novel sensing technique based on these zero-power sensors that enables our vision of high-granularity, maintenance-free and long-lifetime wireless sensor networks for large-scale smart farms with highly efficient water utilization (Fig. 1a).

Zero-standby power IR sensors based on plasmonically-enhanced micromechanical photoswitches (MPs)⁹⁻¹⁵ previously developed by our group, lays the foundation for this work. In contrast to state-of-the-art water stress detectors that constantly consume power and rely on active digitizing electronics, these MPs exploit the energy present in the IR signature emissions from target of interest itself (i.e. the characteristic reflected IR radiation from water-stressed plants) to detect water stress. The MP essentially functions as an IR-triggered electrical switch and by placing the MP between the system battery and active electronics (e.g. a radio transmitter or irrigation valve), (Fig. 1d), the entire system is open-circuited at standby (when the plant is not water stressed) and power consumption is eliminated until the MP is switched ON by the signature IR radiation.

This work reports on a first-of-its-kind non-contact IR-based plant water stress monitoring technique with deployment and maintenance costs potentially orders of magnitude lower than the state-of-the-art, which is ideal for the development of data-driven auto-irrigation systems. It also has minimal complexity in measurement and data processing to accurately determine plant water stress. Since recurring costs are eliminated, this technology is ideal for remote deployment in large-scale crop fields with fine

spatial granularity where it would be implemented as an array of evenly spaced wireless sensor nodes¹⁰.

Design and characterization of the MP

The technique presented here relies on the dependence of the leaf reflectance on the plant water-stress (quantified by the leaf relative water content (RWC)). The leaves of non-water-stressed plants have low reflectance in the SWIR region (1.3 - 1.6 μm) due to strong IR absorption by water in their leaves. When the plant is illuminated by the sun, as shown in Fig. 1b if the leaf is not water-stressed, the sunlight reflected to the MP does not have sufficient power to trigger it ON (i.e. the IR power received by the MP is below its designed threshold), and the system remains completely OFF with zero standby power consumption. However, if the plant is water-stressed, the reflectance increases, and the power received by the MP increases. When it exceeds the power corresponding to a predetermined RWC value (i.e. the designed threshold), the MP turns ON and activates the system to perform a response that can be used to trigger the irrigation system.

The MP presented here has an integrated high-efficiency narrowband plasmonic absorber ($\eta \sim 93\%$, 150 nm bandwidth) that is spectrally-selective to SWIR radiation (1.47 μm) centered at the “water absorption valley” of a leaf’s IR spectra, where there is a significant dependence of reflectance on RWC (Fig. 2a)¹⁶. The MP comprises a pair of symmetric suspended cantilevers, each composed of an IR absorbing (or reflecting) head and an inner and outer pair of thermally sensitive bi-material legs separated by a thermal isolation link as shown in Fig. 2b. The IR absorbing head with the integrated plasmonic absorber selectively converts impinging optical power to heat. Upon the absorption of narrowband SWIR radiation, a large and fast increase of temperature in the corresponding inner pair of legs results in a downward displacement of the cantilever, bringing a high-stiffness platinum (Pt) tip into contact with another contact on the reflector head when the temperature rise is high enough (i.e., when the incident power is above its designed threshold). The working mechanism is described in further detail in⁶. It is worth noting that the switch remains open with a physical gap until it absorbs sufficient SWIR radiation (i.e. its threshold power) reflected from the leaf regardless of the change in ambient temperature, thanks to

ARTICLE

nature
electronics

the symmetric design of the two cantilevers. The sub-micron air gap between the contacts at standby translates directly into zero leakage current and therefore zero-standby power consumption.

A microheater is also integrated on the reflector head to act as a reset function in the event of the contacts getting stuck after closing. Application of a short voltage pulse across the heater causes the

reflector head to thermally actuate downward and away from the absorber head, which reopens the contacts after a detection.

In this work, for the first time, we demonstrate a system-level implementation of a near-zero standby power sensor wherein a commercial off-the-shelf (COTS) water pump is automatically activated when the plant being monitored becomes water-stressed.

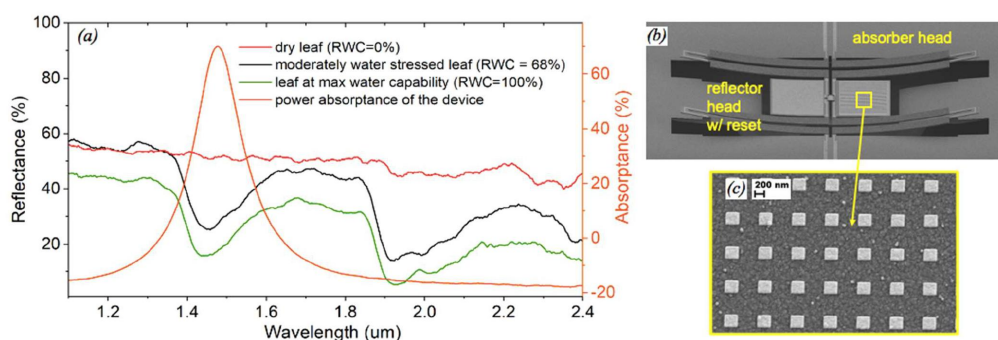


Figure 2. (a) Fourier Transform-IR (FTIR) spectrometer measurement of the spectral absorbance of the fabricated device and of the reflectance of a dry (RWC=0%), moderately water stressed (RWC=68%) and non-stressed (RWC=100%) leaf. Absorption peak of the device perfectly matches the water absorption valley region of the leaf's reflectance spectra. b, SEM image of the fabricated MP. The right cantilever has a SWIR plasmonic absorber while the left one reflects IR and has an in-built microheater for reset. c, Closer look on the absorber.

Reflectance versus RWC

Before performing the tests to demonstrate water-stress detection using the MP, the leaf reflectance was first characterized as a function of its RWC. The experimental setup to characterize a soybean leaf reflectance for varying degrees of water stress is shown in Fig. 3. A circular piece of leaf was chopped from the plant and left overnight in deionized water. This way, the experiment started from the "wet boundary" (its maximum level of water content, where RWC=100%). Once the leaf was removed from the deionized water and pat-dried, it was taped on a circular plastic sample holder. The plastic holder and tape were weighed first without and then with the leaf attached, and for the rest of the experiment the leaf was left attached to the holder (the accurate weight of the leaf was needed to calculate the RWC at each step). The data was collected for the leaf first at the "wet boundary" (0th hour) and then re-measured each successive hour, for five hours. The water-stress was simulated by leaving the leaves in a dry cabinet at 38% humidity. To find their "dry boundary" (RWC = 0%), as a final step in the experiment, they were placed in an oven at -80°C until completely dry and then re-measured. Overall, seven data points were collected for RWC and Reflectance. The experimental setup for the reflectance measurement contained the following:

A light source with a SWIR-transparent diffuser to evenly distribute the light on the leaf.

A Thorlabs S132C power sensor (700-1800 nm range of detection) set to detect at 1550 nm, with 1550 nm bandpass filter (80 nm bandwidth) and a pinhole (which delimits the area of the sensor and simulates an actual MP) at its aperture. It was located perpendicular to the leaf (0° angle), just above the light source. It was connected to a Thorlabs PM100D Power console to record the readings.

An Ocean Optics diffuse reflectance standard (99% reflectance) as reference (the leaf is a diffuse surface).

A sample holder positioned 84 mm far away from the detector. The 99% reflectance reference and the leaf on the holder had approximately the same area (38.75 mm diameter) and were both placed at the same distance (84 mm) with respect to the detector when examined. Each time a power measurement was taken, everything was first removed from the holder and the power detector was zeroed. This way we guaranteed that the power detected from the surroundings was not taken into consideration during the collection of the data. First, the power reflected from the reference was measured knowing that it corresponded to 99% reflectivity. Next the reference was removed from the holder and replaced with the leaf and the power reflected by it was measured. The ratio of the power measured with the leaf to the power measured with the reflectance standard was considered as the reflectance.

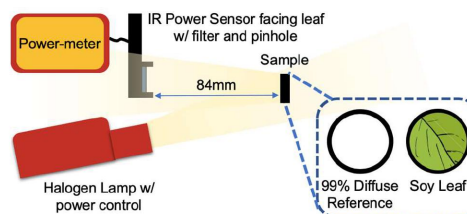


Figure 3. Experimental setup used to measure a soybean leaf reflectance versus its RWC. The setup includes a light source with diffuser, a Thorlabs S132C power sensor, an Ocean Optics diffuse reflectance standard and a sample holder positioned 84 mm from the detector.

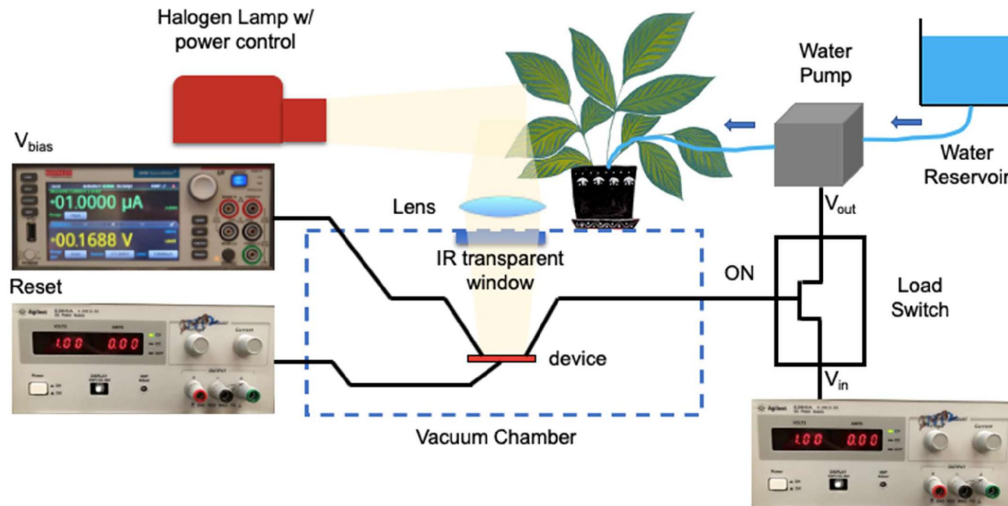


Figure 4. Schematic of the experimental setup used to demonstrate the zero standby power SWIR soybean plant water stress detection. It includes a Quartz tungsten halogen lamp (sunlight simulator), a soybean alive plant, a lens, a vacuum chamber where the MP was placed, a load switch, a water reservoir and a water pump. The MP was connected to a source-meter to apply the V_{bias} and to monitor contact current. It was also connected to a separate DC supply to apply the reset pulse. Another DC supply was used as V_{in} of the load switch. A moderate water-stress condition of the plant (RWC=68%) resulted into the MP closing and, as a consequence, contact current reaching the ON port of the load switch. At that point $V_{out} = V_{in}$ resulting in the activation water pump: 20ml of water released over 20seconds time.

As expected, based on literature, the chopped Soybean leaf dried up very fast: the RWC index dropped rapidly (from 100% to 47.7%) within only one hour of exposure to the dry environment in the Deluxe Smart Grow Closet. In fact, after the first hour the leaf looked already unhealthy (at its wilting point). The measured change in reflectance after the first hour was 4%.

At 1550 nm, literature states that for a Soybean plant the reflectance goes from $\sim 30\%$ reflectance for the wet boundary to $\sim 55\%$ reflectance for the dry one. In our case the measured values go from $\sim 30\%$ to $\sim 49\%$. We consider the results close enough to already existing values and the difference may be caused by the difference in the type/subspecies of Soybean plant.

Since we used a $1.55 \mu\text{m}$ filter with bandwidth of 80 nm, that was available, based on the FTIR measured data, we then extrapolated the values for $1.47 \mu\text{m}$ with bandwidth 150nm (to match our device's absorption). Results are shown in Fig. 5a (red curve).

MP based water-stress detection demonstration

The experimental setup for demonstrating the proposed technique was assembled in a laboratory setting. Fig. 4 shows the setup where a broadband IR illumination source (Quartz tungsten halogen lamp) was used to simulate sunlight. The light was directed towards a leaf on a live soybean plant which was placed on top of a vacuum probe station containing the MP. The leaf was secured on a holder tilted at 45° with respect to the source so as to reflect light to the MP through an IR-transparent window (made of calcium fluoride – CaF₂). A lens on top of the window (also CaF₂) was used to focus the reflected light from the leaf on to the MP. A source meter (Agilent 2450), connected to one end of the MP through a DC probe, was used to apply a bias voltage of 19 V across the contacts while monitoring the switch current. The bias voltage acts as a passive method to scale down the MP's threshold to the required

value¹³. The other end of the MP was linked through a DC probe to the ON pin of an ultra-low leakage load switch (TPS22860). The load switch was used to handle the high current ($\sim 600 \text{ mA}$) drawn by the load (COTS pump) because the MP by itself can handle only up to $200 \mu\text{A}$. The input voltage to the load switch V_{in} was connected to another DC supply set at 5.8V (the pump's operating voltage). The output voltage V_{out} was confirmed to be equal to 0 V when the MP is in the open/standby state and equal to V_{in} when the MP was closed and the ON pin was high. The detailed electrical circuit is described in the supplementary section.

The switch was considered to be ON when the source meter reading abruptly changed from $\sim 10 \text{ nA}$ (i.e. noise floor) to $\sim 10 \mu\text{A}$ (internally limited). A 1 V pulse ($\sim 100 \text{ ms}$) from a separate DC source applied to the reset heater ($R \sim 50 \text{ k}\Omega$) was used to reopen the contacts to guarantee repeatable testing.

The IR power reflected from a soybean leaf with varying RWC was first characterized by substituting the MP in the experimental setup (Fig. 4) with a commercial IR sensor, from which the required MP threshold was found to be $\sim 209 \text{ nW}$ corresponding to an initial water-stressed state (RWC=68%). This RWC was chosen as the initial water-stressed level since the plant was still in an easily recoverable state if watered. The fabricated MP was then placed in the chamber and fine-tuned to have a threshold of 209 nW by applying a bias voltage⁹. The MP was then sequentially exposed to the soybean plant with RWC decreasing from 100% to 25% while the current in the device was monitored. As expected, the device reliably turned ON only when exposed to samples with $\text{RWC} \leq 68\%$ as shown by the abrupt (> 5 order of magnitude) current change in Fig. 5a (blue curve). The device remained completely off with zero standby leakage (instrument noise limited to $\sim 10^{-5} \mu\text{A}$) for higher RWCs as required. Using the source meter, an overall system current of $\sim 500 \text{ mA}$ was measured when the MP was triggered ON

ARTICLE

nature
electronics

and the pump was activated, and only ~ 180 nA when the MP was off, and the system was at standby. It is notable that this represents a >160 times improvement over the standalone pump which operated on a duty-cycle and had a standby current of $28.4 \mu\text{A}$.

It is also worth noting that even though the reflectance change in the range from 100% RWC to 68% RWC is only 3.2%, the device is able to differentiate between the IR power levels at these two RWCs. As a test for repeatability, Fig. 5c shows the measured current through the MP in response to chopped IR radiation reflected off the water stressed leaf at RWC = 68%. Due to the pull-in voltage effect, the MP latches ON after each detection. To reopen the switch for the next detection, a 1V pulse (~ 100 ms) applied to the reset heater ($\sim 50\text{k}\Omega$) returns the switch to an open and OFF state until triggered ON again by above-threshold IR when the shutter is removed from the top of the vacuum chamber's window. Each time the MP is triggered ON the water pump turns on as shown in Fig. 5d.

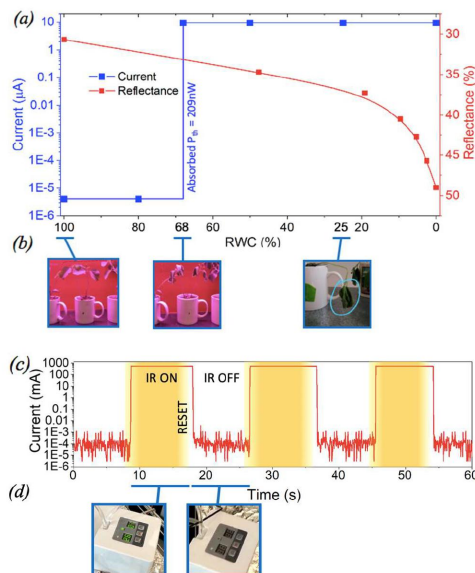


Figure 5. (a) Experimental result of the current flowing through the MP and reflectance of the leaf as a function of the relative water content (RWC) of the leaf. (b) The tested soybean alive plant at different RWCs (100%, 68%, and 0%). (c) Measured current through the MP in response to chopped IR radiation reflected off the leaf at RWC = 68%. The MP latches ON after each detection and the reset function returns the switch to an OFF state until triggered ON again by above-threshold IR. (d) The water pump turns ON state when the MP closes as a response to IR radiation reflected off the leaf at RWC=68%. After the reset, the water pump remains OFF until triggered ON again by above-threshold IR.

Characterization of Wilting Point and Maximum Reflectance Change for Recoverability

An additional experiment was performed in order to identify the minimum RWC for which, if a plant is watered, it recovers fully (i.e. its water-stressed wilting point). This form of irrigation where the plant is irrigated at its maximum stress point is called 'deficit irrigation' and represents the case where maximum water savings is

required, though yield may be reduced. This case would also correspond to the maximum reflectance change that can be targeted by the sensor. Five plants with an initial state of 100% RWC each in its own pot, were observed. With time, the RWC gradually lowered due to natural evapotranspiration and the first plant was watered at an RWC=63%, whereupon it was found to recover to its full RWC of 100%. By the time the second plant was watered its RWC was 57%. This plant also successfully recovered. This process was subsequently repeated for the next three plants (at RWC of 50%, 47% and 35%). It was found that the last two did not recover upon watering them and thus it was concluded that the minimum RWC for which, if watered, a plant recovers is 50%. This corresponds to a leaf reflectance change of 5% and is expected to be the upper limit of detection for our sensors. Thus if the aim is minimize water usage to the maximum extent, the MP can be tuned to turn on at RWC=50%. However, if the aim is to reach a tradeoff between maximizing the yield and reducing water consumption, then it would better to tune the MP to turn on at a higher RWC of 68%¹⁷.

Impact on Optimization of water usage

A crop's water usage is strongly influenced by its stage of growth. When a soybean plant does not receive enough water to meet evapotranspiration demands during the reproductive growth stages, significant reductions in yield can occur. A Soybean's water requirements change throughout its lifetime (about 130 days) over different stages of growth¹⁷: the first 20 days of germination and seedling require 0.05 inches water per day, the following 30 days of rapid vegetative growth require 0.10 inches water per day, the next 30 days of flowering to early pod require 0.20 inches water per day, the next 30 days of pod development to pod fill require 0.25 inches water per day and finally the last 20 days from maturity to harvest require as few as 0.05 inches water per day. By tuning the MP to be able to detect water stress when still at a mildly-stressed stage, not to compromise the yield (RWC=60 to 70%), about 10,000 gallons would be used per bush over a lifetime which would correspond to what is currently achieved through the innovative water management oriented methods.

Each additional acre-inch of water results in an approximate yield gain of 10 bushels/acre for corn and 3 bushels/acre for soybeans. Thus every little bit of water can have a significant effect on final grain yield¹⁸.

In-Field simulation - analytical model

An analytical model was also developed to assess the feasibility of deployment of the demonstrated water-stress sensor in a crop field. Here the required threshold power of an MP for a targeted reflectance (corresponding to a water-stressed leaf) was calculated as a function of distance based on the IR radiant heat transfer equations described in¹⁹. This model was validated experimentally as described in the supplementary section. Fig. 5 shows the predicted power reaching the MP as a function of distance from a water-stressed soybean leaf. The analytical model developed to obtain this graph considers the leaf as a diffuse reflector having a reflectance of 33.4% for an RWC = 68%. Solar irradiance in the targeted SWIR band (28.3 W/m^2 from²⁰) and a circular leaf region of 0.5m radius are considered to simulate a realistic scenario. The model also incorporates atmospheric attenuation of SWIR by water vapor. No converging optics were included in the model. The result shows that for an MP threshold of 209 nW, the device needs to be placed 0.75m from the leaves to detect a water stress level of RWC = 68%.

ARTICLE

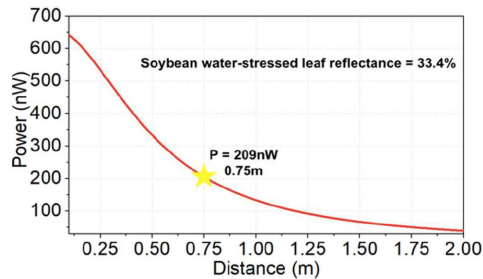
nature
electronics

Figure 5. Predicted power reaching the MP as a function of distance from a leaf. For an MP threshold of 209nW, the device needs to be placed 0.75m from the leaves to detect a water stress level of RWC=68%.

Conclusions

A new technique for standoff detection of plant water-stress using zero standby power MPs was experimentally demonstrated. The proposed MEMS-based passive water-stress sensor technology shows great potential for the realization of persistent zero-power crop water-stress sensor networks.

According to the prioritization of yield or water consumption, the MP can be tuned to water the crop upon detection of mild to severe water-stress conditions. The standby power consumption of the water pump is proven to be improved by 160 times through its integration with the MP.

Furthermore, the MP would be able to reduce water usage on rainy days since the plant's water stress will be alleviated, thereby reducing even more the amount of water that needs to be provided by the farmer in a completely automated way. This is especially effective as compared to manual or duty-cycled techniques that cannot perform 'need-based' irrigation.

The drastically increased sensor lifetime paves way for an unprecedented scale of deployment of sensor nodes for high granularity, maintenance-free networks suitable for large-scale farms.

Methods

Fabrication of the MP. The key features of the switch structure are as follows: (a) The plasmonic absorber on one cantilever head and a gold (Au) reflector on the other, (b) a bowl-shaped Pt contact, (c) bi-material beams and (c) an embedded microheater under the reflector head for reset function. The plasmonic absorber comprises a metal-insulator-metal stack made of a bottom reflector (5-50-nm thick Ti-Pt-Ti), a thin dielectric spacer (50 nm thick SiO₂) and an array of Au patches (5-50-nm thick Ti-Au-Pt nanostructures) whose absorption wavelength can be tuned lithographically¹³. The absorber head also has a bowl-shaped high-stiffness Pt contact tip for repeatable ON-OFF switching. The Pt contact tip is electrically connected to one of the device terminals, while the other terminal is connected to the lower contact pad on the reflector head. The Pt tip and the contact pad are separated by an air gap which closes when an infrared radiation, with power exceeding the designed threshold and that matches the lithographically defined absorption band ($\lambda = 1.47 \mu\text{m}$), is absorbed by the device. The reflector head has the purpose of ambient temperature compensation and helps maintain the contact gap due to common-mode inputs such as ambient temperature changes and residual stress. This Ohmic loss is conducted to the bi-material inner legs and it stops at the thermal isolation. The heat causes the downward bending of the inner legs and the consequent vertical displacement of the upper head puts in contact the Pt tip to the contact pad on the opposite head. Any other unwanted deflection, for example the change in ambient temperature, is compensated by the two outer legs due to the symmetry of the structure.

A 13-mask microfabrication process was used to fabricate the new reflectance-based water-stress sensors, which included one mask-less step of electron-beam lithography for the plasmonic absorber. The fabrication process flow is described in further detail in⁶ with the difference of the integration, as a first deposited layer, of a new reset functionality through a heater in the lower

head, as well as a customized lithographic tuning of the absorber to detect water-stress in the leaf. A high resistivity 4-inch Si wafer was selected to enable the use of the bottom heater without current leakage through the substrate.

Plant selection and growing conditions. We chose to perform our tests on Soybean (*Glycine Max*) due to its fast growth rate, quick response to water-stress and large amount of relevant data available in literature. The soybean plant was grown in an enclosed Delux Smart Grow Closet in our lab, which was fitted with air filters (to avoid cross-contamination between the lab and closet), continuous airflow, a thermo/hygrometer and grow lights. The hygrometer, a thermometer and a Kind LED K3 Series 2 XL450 grow light allowed us to keep the plant under constant humidity (~30%) and temperature (~26°C) as well as to enable perpetual growing cycles. A DIY Micro Automatic Drip Irrigation Kit was used to water the plants daily (300 ml/day).

Design rationale for the circuit. A commercial DIY Micro Automatic Drip Irrigation Kit operating at 5.8 V was used to supply water to the soybean plant when water-stressed. Connecting it to the source meter as the power supply allowed us to measure the current while it was operating. In order to integrate the water pump in the system, three Texas instruments TPS22860 Ultra Low-Leakage Load Switches, each with a maximum current capacity of 200 mA, were stacked in parallel to handle the 600 mA current requirement of the pump. The ON/OFF input of the load switch was connected to the MP through a simple voltage divider composed of a 1.5 M Ω resistance connected to the voltage coming from the MP (19 V when closed, 0 V when open) and a 470k resistance connected to ground. The output of the voltage divider (6 V when closed, 0 V when open) was connected to the ON/OFF input of the load switch. The V_{in} pin of the load switch was connected to a DC supply providing 5.8 V and a current limited to 600 mA not to damage the load switch. Finally, by connecting the V_{out} pin of the load switch to the water pump, whenever the MP detected water-stress in the plant and closed, the ON input received 6 V changing V_{out} from 0 V to become equal to V_{in} eventually resulting in the activation of the pump and the plant being watered.

RWC as a measure of water stress. Among the many indices used in literature to model reflectance spectra versus the water content of the leaf, we chose the Relative Water Content (RWC) for two main reasons. Firstly, it is relatively easy to obtain directly from the weight of the leaf (directly dependent on the leaf water content) and is easy to calculate. The second reason is because we found consistent RWC literature connecting the reflectivity of *Glycine Max* to its water content therefore allowing a solid comparison of our results with results of already existing techniques.

The measurements were done with circular cut leaf discs of 3 cm diameter (We avoided large veins when cutting). The formula used was: $RWC (\%) = [(W - DW) / (TW - DW)] * 100$ where W = weight of the cut leaf disc, TW is the weight of the leaf disc after being immersed in water in a closed petri dish to reach full turgidity in 3-4h under normal lab conditions (we measured $TW = 0.126 \text{ g}$), DW is the mass of the leaf disc dried at 800C for 24h and weighed (measured $DW = 0.015 \text{ g}$).

Generally, the RWC was 98% for fully turgid transpiring leaves, 60% to 70% for the initial wilting stage and 30% to 40% for severely desiccated and dying leaves.

Data availability. The data that support the plots within this paper and other findings of this study are available from the corresponding authors upon reasonable request.

Received: 28 August 2020; Accepted: _____;

Published online: _____

References

- How to Feed the World in 2050: http://www.fao.org/fileadmin/templates/wfs/docs/expert_paper/How_to_Feed_the_World_in_2050.pdf
- Samuel O. Ihuoma, Chandra A. Madramootoo, "Recent advances in crop water stress detection", *Computers and Electronics in Agriculture*, Volume 141, 2017, Pages 267-275.
- A Survey on the Role of IoT in Agriculture for the Implementation of Smart Farming: <https://ieeexplore.ieee.org/stamp/stamp.jsp?arnumber=8883163>
- Is There an AgTech Bubble? <http://fortune.com/2016/07/25/agriculture-farming-tech-startup-bubble/>
- A. Gard, P. Munoth, R. Goyal, "APPLICATION OF SOIL MOISTURE

- SENSORS IN AGRICULTURE: A REVIEW”, in 2016 International Conference on Hydraulics, Water Resources and Coastal Engineering.
6. S. Datta, S. Taghvaeian, T. E. Ochsner, D. Moriasi, P. Gowda, and J. L. Steiner, “Performance Assessment of Five Different Soil Moisture Sensors under Irrigated Field Conditions in Oklahoma” in *Sensors (Basel)* 2018.
 7. R. H. Olsson, R. B. Bogoslovov, and C. Gordon, “Event driven persistent sensing: Overcoming the energy and lifetime limitations in unattended wireless sensors,” in 2016 IEEE SENSORS, 2016, pp. 1–3.
 8. Z. Qian, S. Kang, V. Rajaram, C. Cassella, N. E. McGruer, and M. Rinaldi, “Zero-power infrared digitizers based on plasmonically enhanced micromechanical photoswitches,” *Nat. Nanotechnol.*, vol. 12, no. 10, pp. 969–973, Sep. 2017.
 9. Z. Qian, S. Kang, V. Rajaram, C. Cassella, N. E. McGruer, and M. Rinaldi, “Zero-power light-actuated micromechanical relay,” in *IEEE MEMS*, 2017, pp. 940–941.
 10. V. Rajaram, Z. Qian, S. Kang, and M. Rinaldi, “MEMS- Based Near-Zero Power Infrared Wireless Sensor Node,” in *IEEE MEMS*, 2018, pp. 17–20.
 11. V. Rajaram, Z. Qian, S. Kang, C. Cassella, N. E. McGruer, and M. Rinaldi, “Microelectromechanical detector of infrared spectral signatures with near-zero standby power consumption,” in 19th International Conference on Solid-State Sensors, Actuators and Microsystems (TRANSDUCERS), 2017, pp. 846–849.
 12. S. Kang, Z. Qian, V. Rajaram, A. Alu, and M. Rinaldi, “Ultra narrowband infrared absorbers for omni-directional and polarization insensitive multi-spectral sensing microsystems,” in 19th International Conference on Solid-State Sensors, TRANSDUCERS, 2017, pp. 886–889.
 13. V. Rajaram, Z. Qian, S. Kang, S. D. Calisgan, N.E. McGruer, and M. Rinaldi, “Zero-Power Electrically Tunable Micromechanical Photoswitches”, *IEEE Sensors Journal*, 2018, DOI: 10.1109/JSEN.2018.2850898.
 14. Z. Qian, V. Rajaram, S. Kang, and M. Rinaldi, “High Figure-of-Merit NEMS Thermal Detectors based on 50-nm Thick AlN Nano-Plate Resonators”, *Applied Physics Letter*, vol.115, issue 26, Dec. 2019, 10.1063/1.5128643
 15. S. Kang, Z. Qian, V. Rajaram, S. D. Calisgan, A. Alu’, and M. Rinaldi, “Ultra-narrowband Metamaterial Absorbers for High Spectral Resolution Infrared Spectroscopy”, *Advanced Optical Materials*, vol. 1801236, p. 1801236, Nov. 2018. doi:10.1002/adom.201801236
 16. William J. Ripple, “Spectral Reflectance Relationships to Leaf Water Stress”, *Photogrammetric Engineering and Remote Sensing*, Vol. 52, No. 10, October 1986, pp. 1669-1675.
 17. Water Use in Soybean and Irrigation Timing: <https://www.krugerseed.com/en-us/agronomy-library/water-use-in-soybean-and-irrigation-timing.html#:~:text=Soybeans%20require%20approximately%2015%20inches%2C%20location%2C%20and%20weather%20conditions.&text=The%20most%20important%20time%20to,%2D%20to%20late%2Dproductive%20stages.>
 18. Drip irrigation and fertigation: http://cropphysiology.croplsci.illinois.edu/research/drip_irrigation.html
 19. Heat Transfer And Thermal Radiation Modeling: <http://webserver.dnt.upm.es/~isidoro/tc3/Heat%20transfer%20and%20thermal%20radiation%20modelling.pdf>
 20. Reference Solar Spectra Irradiance: Air Mass 1.5 <https://rredc.nrel.gov/solar/spectra/am1.5/>

Acknowledgments

The authors would like to thank the staff of the George G. Kostas Nanoscale Technology and Manufacturing Research Center at Northeastern University, Boston. The project described was funded by the ARPA-E OPEN Smart Farm Program, Grant no. G00006135.

Competing interests

The authors declare no competing interests.

Appendix C

Matlab Minicode

The following code is used for the power threshold calculation of the temperature-based IR sensor, changing the distance between the leaf and the device.

```
1  clc;
2  clear all;
3  close all;
4
5  R=0.5; %half width of area of the leaves
6  Ao=pi*R^2; %area of the leaves (m^2)
7  H=1; %distance between leaves and detector (m)
8  As=150*150e-12; %area of the head of the detector
9  dT=0:0.1:7; %change in temperature (steps)
10
11 Te=298; %environment temp
12 To=Te+dT;
13
14 Gcon=1.15e-6; %thermal conductivity of the device
15 k=As*Ao.*0.648/(R^2+H.^2); %equation from page 50 of one of the docs
16 Ts=(k.*To+Gcon*Te)/(k+Gcon); %equations from other document
17 Pt=Gcon.*(Ts-Te)/10^-9; %threshold power for temperature sensor
18 plot(dT,Pt);
19 xlabel('Decrease in temperature related to decrease of water stress (
    C)');
20 ylabel('Power (nW)');
```

Bibliography

- [1] FAO. *How to feed the world in 2050*. URL: http://www.fao.org/fileadmin/templates/wsfs/docs/expert_paper/How_to_Feed_the_World_in_2050.pdf (cit. on pp. ii, 2).
- [2] Zhenyun Qian, Sungho Kang, Vageeswar Rajaram, Cristian Cassella, Nicol E McGruer, and Matteo Rinaldi. «Zero-power infrared digitizers based on plasmonically enhanced micromechanical photoswitches». In: *Nature nanotechnology* 12.10 (2017), pp. 969–973 (cit. on pp. ii, 2, 3, 6, 18, 19).
- [3] *NSandNS Laboratory*. URL: <https://web.northeastern.edu/nemslab/> (cit. on p. 1).
- [4] Richard E Smart and Gail E Bingham. «Rapid estimates of relative water content». In: *Plant physiology* 53.2 (1974), pp. 258–260 (cit. on p. 6).
- [5] Farm Energy. *Soybeans for Biodiesel Production*. URL: <https://farm-energy.extension.org/soybeans-for-biodiesel-production/#:~:text=One%5C%20bushel%5C%20of%5C%20soybeans%5C%20can,5.1%5C%20billion%5C%20gallons%5C%20of%5C%20biodiesel> (cit. on p. 11).
- [6] E Raymond Hunt Jr and Barrett N Rock. «Detection of changes in leaf water content using near-and middle-infrared reflectances». In: *Remote sensing of environment* 30.1 (1989), pp. 43–54 (cit. on p. 14).
- [7] Sila Deniz Calisgan, Vageeswar Rajaram, Zhenyun Qian, Sungho Kang, Antea Risso, and Matteo Rinaldi. «Zero-Power Chemical Sensor Based on a Polymer/Metal Micromechanical Switch». In: *2019 IEEE SENSORS*. IEEE, 2019, pp. 1–4 (cit. on p. 16).
- [8] Texas Instruments. «Low-Power PIR Motion Detector With Sub-1GHz Wireless Connectivity Enabling 10-Year Coin Cell Battery Life». In: (2016) (cit. on p. 17).
- [9] Christian Ranacher et al. «A CMOS Compatible Pyroelectric Mid-Infrared Detector Based on Aluminium Nitride». In: *Sensors* 19.11 (2019), p. 2513 (cit. on pp. 17, 18).

- [10] Antoni Rogalski. «Infrared detectors: status and trends». In: *Progress in quantum electronics* 27.2-3 (2003), pp. 59–210 (cit. on p. 18).
- [11] Dehui Xu, Yuelin Wang, Bin Xiong, and Tie Li. «MEMS-based thermoelectric infrared sensors: A review». In: *Frontiers of Mechanical Engineering* 12.4 (2017), pp. 557–566 (cit. on p. 18).
- [12] Ali Attaran and Rashid Rashidzadeh. «Ultra low actuation voltage RF MEMS switch». In: *Micro and Nano Systems Letters* 3.1 (2015), p. 7 (cit. on p. 18).
- [13] WILLIAMJ RIPPLE. «Spectral reflectance relationships to leaf water stress». In: *Photogrammetric Engineering and Remote Sensing* 52.10 (1986), pp. 1669–1675 (cit. on p. 19).
- [14] C Lin, SC Popescu, SC Huang, PT Chang, and HL Wen. «A novel reflectance-based model for evaluating chlorophyll concentrations of fresh and water-stressed leaves». In: *1foldr Import 2019-10-08 Batch 5* (2015) (cit. on p. 19).
- [15] Zhenxing Cao, Quan Wang, and Chaolei Zheng. «Best hyperspectral indices for tracing leaf water status as determined from leaf dehydration experiments». In: *Ecological indicators* 54 (2015), pp. 96–107 (cit. on p. 19).
- [16] Saleem Ullah, Andrew K Skidmore, Abel Ramoelo, Thomas A Groen, Mohammad Naeem, and Asad Ali. «Retrieval of leaf water content spanning the visible to thermal infrared spectra». In: *ISPRS journal of photogrammetry and remote sensing* 93 (2014), pp. 56–64 (cit. on pp. 19, 20).
- [17] Jennifer Alsever. *Is There an AgTech Bubble?* URL: <http://fortune.com/2016/07/25/agriculture-farming-tech-startup-bubble/> (cit. on p. 20).
- [18] National Renewable Energy Laboratory. *Solar Resource Data and Tools*. URL: <https://www.nrel.gov/grid/solar-resource/renewable-resource-data.html> (cit. on pp. 22, 54).
- [19] *Solar Cell*. KXOB22-01X8F. IXYS Corporation. 2016. URL: https://ixapps.ixys.com/DataSheet/KXOB22-01X8F_Nov16.pdf (cit. on p. 25).
- [20] PVEducation. *Ideality Factor*. URL: <https://www.pveducation.org/pvcdrom/solar-cell-operation/ideality-factor#:~:text=Ideality%5C%20Factor-,Ideality%5C%20Factor, follows%5C%20the%5C%20ideal%5C%20diode%5C%20equation.&text=In%5C%20practice%5C%2C%5C%20there%5C%20are%5C%20second, a%5C%20way%5C%20of%5C%20describing%5C%20them.> (cit. on p. 26).
- [21] Javier Cubas, Santiago Pindado, and Carlos De Manuel. «Explicit expressions for solar panel equivalent circuit parameters based on analytical formulation and the Lambert W-function». In: *Energies* 7.7 (2014), pp. 4098–4115 (cit. on pp. 26, 28).

-
- [22] Faisal Ghani, G Rosengarten, Mike Duke, and JK Carson. «The numerical calculation of single-diode solar-cell modelling parameters». In: *Renewable Energy* 72 (2014), pp. 105–112 (cit. on p. 26).
- [23] Chuck Wright. *Measuring solar radiation*. URL: <http://www.chuck-wright.com/projects/pv-measure.html> (cit. on p. 28).
- [24] *Low Power Step Up Voltage Regulator*. TPS61096. Texas Instruments. 2017. URL: <https://www.ti.com/lit/ds/symlink/tps61096a.pdf?ts=1590681536782> (cit. on pp. 30, 35).
- [25] *Low Power Regulator*. LTC1307. Linear Technology. URL: <https://www.analog.com/media/en/technical-documentation/data-sheets/1307fa.pdf> (cit. on pp. 29, 35).
- [26] *Low Power Window Comparator*. LTC1042. Linear Technology. URL: <https://www.analog.com/media/en/technical-documentation/data-sheets/1042fa.pdf> (cit. on pp. 32, 34, 35, 45).
- [27] *What it is, what it isn't, and how to use it*. Texas Instruments. URL: <https://www.ti.com/lit/an/slyt412/slyt412.pdf> (cit. on p. 41).
- [28] *256-Position, Ultralow Power 1.8 V Logic-Level Digital Potentiometer*. AD5165. Analog Devices. URL: <https://www.analog.com/media/en/technical-documentation/data-sheets/AD5165.pdf> (cit. on p. 43).
- [29] Vageeswar Rajaram, Zhenyun Qian, Sungho Kang, Sila Deniz Caliskan, and Matteo Rinaldi. «MEMS-Based Battery-Less RFID Infrared Sensor Tag with Memory Function». In: *2019 IEEE 32nd International Conference on Micro Electro Mechanical Systems (MEMS)*. IEEE. 2019, pp. 266–269 (cit. on p. 53).
- [30] Vageeswar Rajaram, Zhenyun Qian, Sungho Kang, Nicol E McGruer, and Matteo Rinaldi. «MEMS-based near-zero power infrared wireless sensor node». In: *2018 IEEE Micro Electro Mechanical Systems (MEMS)*. IEEE. 2018, pp. 17–20 (cit. on p. 53).
- [31] Texas Instruments. *Basics of Load Switches*. URL: https://www.ti.com/lit/an/slva652a/slva652a.pdf?ts=1594935325063&ref_url=https%5C%253A%5C%252F%5C%252Fwww.google.com%5C%252F#:~:text=Integrated%5C%20load%5C%20switches%5C%20are%5C%20electronic,to%5C%20implement%5C%20with%5C%20discrete%5C%20components. (cit. on p. 55).
- [32] *TPS22860 Ultra-Low Leakage Load Switch*. TPS22860. Texas Instruments. URL: https://www.ti.com/lit/ds/symlink/tps22860.pdf?ts=1594928848484&ref_url=https%5C%253A%5C%252F%5C%252Fwww.google.com%5C%252F (cit. on p. 56).